Skill Assessment of NCEP Three-Way Coupled HWRF–HYCOM–WW3 Modeling System: Hurricane Laura Case Study

HYUN-SOOK KIM,[a,b] JESSICA MEIXNER,[c] BIJU THOMAS,[a,c] BRANDON G. REICHL,[d] BIN LIU,[a,c] AVICHAL MEHRA,[c] AND ALAN WALLCRAFT[e]

[a] *IMSG at NOAA/NCEP/EMC, College Park, Maryland*
[b] *NOAA/Atlantic Oceanographic and Meteorological Laboratory, Miami, Florida*
[c] *NOAA/Environmental Modeling Center, College Park, Maryland*
[d] *NOAA/Geophysical Fluid Dynamics Laboratory, Princeton, New Jersey*
[e] *Center for Ocean–Atmospheric Prediction Studies, Florida State University, Tallahassee, Florida*

(Manuscript received 30 November 2021, in final form 4 April 2022)

ABSTRACT: In this research, we develop a three-way coupled prediction system to advance the realization of air–sea interaction processes. This study considers the sea-state-dependent momentum flux and nonlinear interactions between waves, winds, and ocean currents using the U.S. National Centers for Environmental Prediction's operational Hurricane Weather Research and Forecasting (HWRF)-Hybrid Coordinate Ocean Model (HYCOM) coupled modeling system. Wave feedback is performed through the air–sea interaction module (ASIM) added to WAVEWATCH III (WW3), which employs the wave boundary layer to parameterize unresolved high-frequency tail spectra by using the mean flux profile constructed from the conservation of total momentum and wave energy. The atmospheric momentum flux is updated using the sea-state-dependent Charnock coefficient, wave-induced stress, and ocean surface currents before being passed to HYCOM. Wave coupling in HYCOM includes Coriolis–Stokes forcing to simulate wave–current interactions and to enhance mixing to account for Langmuir turbulence. The fully coupled system is tested for Hurricane Laura (2020). This paper examines the forecast skills of the individual component models by comparing simulations with observations. Without skill degradation of HYCOM and WW3, the three-way coupling method improves the track and intensity forecast skills by 5% each over those of HWRF-HYCOM coupling, and 27% and 17% over those of uncoupling, respectively. Importantly, this fully coupled system outperforms rapid intensification by reducing the intensification magnitude and matching the occurrence and duration. Overall, the forecast performance evaluated in the study establishes a baseline for the next-generation hurricane prediction system.

SIGNIFICANCE STATEMENT: This study is the documentation of the numerical advancement of tropical cyclone (TC) forecasting and the demonstration of the improvement of the TC intensity forecast. A key asset is the importance of wave coupling and inclusion of the nonlinear interactions in the air–sea interaction zone, and is to advance the current U.S. NCEP operational coupled hurricane modeling system. By assessing simulations for Hurricane Laura (2020), we demonstrate skill improvement of the storm structure, and intensity forecasts, especially for rapid intensification (RI) by correcting the timing and the magnitude of RI simulated by uncoupling and two-way coupling.

KEYWORDS: Air-sea interaction; Mesoscale processes; Oceanic waves; Wind waves; Mixing; Upwelling/downwelling; Tropical cyclones; Coupled models; Short-range prediction

1. Introduction

Tropical cyclone (TC) numerical weather prediction depends on the accurate representation of the flux exchange of momentum, heat, and moisture at the air–sea interaction zone. A TC draws heat energy from the ocean and converts it to mechanical energy to sustain or abate its intensity. The underlying process is sea surface temperature (SST) feedback, which closes the thermodynamic loop between the atmosphere and the ocean as one Earth system. Air–sea interaction processes, however, are more complex than a simple SST feedback process. The processes are highly nonlinear and predominated by spatiotemporal multiscale turbulence (Black et al. 2007; Chen et al. 2007; Edson et al. 2007). Much progress has been made in the scientific understanding of air–sea–wave interactions over the past 30 years (Hagos et al. 2020), but this remains a relatively less explored area in TC prediction.

To date, the current practice in operational TC numerical weather prediction (NWP) is based on two-way dynamic ocean–atmosphere coupled models—e.g., the Geophysical Fluid Dynamics Laboratory hurricane model (Bender et al. 2007), the National Centers for Environmental Prediction (NCEP) Hurricane Weather Research and Forecasting (HWRF) Model (Kim et al. 2014; Tallapragada 2016), the Hurricane Multi-Scale Ocean-coupled Non-Hydrostatic Model (Mehra et al. 2018), the U.S. Navy's Coupled Ocean–Atmosphere Mesoscale Prediction System for Tropical Cyclones (Doyle et al. 2012; 2014), and the Tropical Cyclone Limited Area Prediction System (Sandery et al. 2010). This approach generally uses the same bulk parameterization of turbulent exchange fluxes as that used for non-coupled modeling. A first step taken to advance the

Corresponding author: Hyun-Sook Kim, hyun.sook.kim@noaa.gov

DOI: 10.1175/WAF-D-21-0191.1

coupled HWRF model is to explicitly include waves for better representation of the air–sea interaction processes, the coevolution of the atmospheric and oceanic state, and also improvements in predictability.

Under a moving TC, the generation of ocean surface gravity waves poses different levels of complexity beyond the capabilities of the current U.S. NCEP operational NWP models. In the presence of gravity waves, airflow becomes rougher. Hence, these waves are more efficient in extracting momentum flux from the air. Due to the time variations in TC intensity and transit speed, the waves induced by the TC can be fetch and duration limited. In the conditions, the atmosphere–ocean momentum exchange is further modulated by waves through sea state, wave-induced stress, wave–wave, wave–wind, and wave–current interactions. However, oceanic and atmospheric models use a constant Charnock coefficient to parameterize surface roughness (Charnock 1955), including hurricane wind speeds exceeding 30 m s^{-1} (Kurihara et al. 1998). Wave-induced stress is primarily governed by the high-frequency part of the wave spectrum and has the largest growth rate in high-wind conditions (Donelan et al. 2004) or magnitude greater than 15 m s^{-1} (Tolman 2014). However, the current state-of-the-art numerical wave models are unable to accurately resolve the high-frequency part of the wave spectrum. For this reason, models employ parameterizations for high-frequency components using, for instance, momentum and energy conservation (Hara and Belcher 2002; Moon et al. 2004a,b; Reichl et al. 2016), an energy balance model (Kudryavtsev and Makin 2001; Makin and Kudryavtsev 2002), or a unified velocity structure (Bye and Wolff 2008).

In our study, we used the NCEP WAVEWATCH III (WW3) model with the air–sea interaction module (ASIM) developed at the University of Rhode Island as a submodule for wind–wave coupling (Moon et al. 2004a,b; Reichl et al. 2016). An underlying assumption used in the calculation of wave-induced stress is the conservation of wave energy and momentum in the wave boundary layer to support the mean wind profile. Total stress in the boundary layer is the sum of wave-induced stress and turbulence that matches the atmospheric momentum flux at the top of the wave boundary layer. These unresolved stresses are estimated through tail spectrum parameterization, which includes the impact of waves on the inner height, such as the wave growth rate, the misalignment between wind and stress, and the parameterized effects of wave breaking (see details in Reichl et al. 2014, hereafter R14). Doyle (2002) and Chen et al. (2013) both developed and demonstrated a three-way hurricane–ocean–wave coupling system for real cases. Although they employed different methods for the wave-induced stress estimates by applying either a simple roughness length scale as a function of the total and wave-induced stress (Doyle 2002) or empirically determined the short-wave spectrum based on a logarithmic wind profile (Chen et al. 2013), the objectives of these studies were similar to our present study. However, their approaches excluded the relative effects of ocean currents on the atmospheric wind and nonlinear interactions between waves and ocean currents. Our study explicitly not only includes resolved ocean current–wave interactions and ocean current–wind interactions but also includes the effects of Langmuir turbulence on the parameterized ocean surface boundary layer mixing in the ocean circulation model.

Although it is still difficult to make quantitative measurements of flux exchange and also is not well understood in terms of the fundamental physics, the importance of the feedback in the air–sea interaction zone has long been recognized in the development of atmospheric mesoscale variations (Small et al. 2008; Song 2021; Renault et al. 2016; Sweet et al. 1981). Recently, the numerical approach has been raised to increasing levels of coupling submodels and physics (e.g., Liu et al. 2011; Porchetta et al. 2020; Zambon et al. 2014; Xu et al. 2021; Zambon et al. 2021). These methods are based on NWP systems that are more sophisticated and include different component models from those of operational numerical models. But, they provide new or improved knowledge and technologies to apply in numerical guidance models. We present our efforts on full hurricane–ocean–wave coupling using the operational HWRF system and assess the prediction performance for essential features in each submodel. The outline of the present paper is as follows: an introduction of the coupled modeling system is presented in section 2, its application in section 3, the results in section 4, and a summary and conclusions in section 5.

2. Coupled modeling system

The coupled modeling system used in this study is based on version 13.1 of HWRF, which provided operational numerical guidance for the 2021 season TC forecasts. The major components of the system include the HWRF Model, the Hybrid Coordinate Ocean Model (HYCOM), and WW3. The wave coupling allows interacting with the surface boundary layer model of the atmospheric model component (Moon et al. 2004a,b; R14). For there to be wave–ocean interactions, HYCOM employs a Stokes drift module that recognizes wave–current interactions and Langmuir turbulence mixing. Figure 1 shows a schematic of the three-way HWRF modeling system, with coupling variables and the directions of the flow of information between the model components. Coupling communications are conducted through the NCEP coupler that passes exchange variables after interpolation/extrapolation.

The atmospheric model component is configured with two moving nests that follow a storm at fine horizontal resolutions and a quasi-static outer domain at a coarse resolution that provides estimates of basin-scale environmental dynamics and physics (Fig. 2). HYCOM and WW3 cover a transatlantic region extending from 5° to 45°N in latitude at a resolution of 1/12° on a Mercator projection and rectangular coordinates, respectively. Prognostic variables over unmapped areas of the HWRF outer domain are substituted with the initial condition values persistently over the entire forecast period, and the HYCOM unmapped region are prescribed with time-variant global forecast system (GFS) forcing.

For the very first cycle, HWRF starts from a cold start that is based on the NCEP GFS analysis through remapping onto the rotated-Earth coordinates in the horizontal direction and the sigma-pressure hybrid layers in the vertical, followed

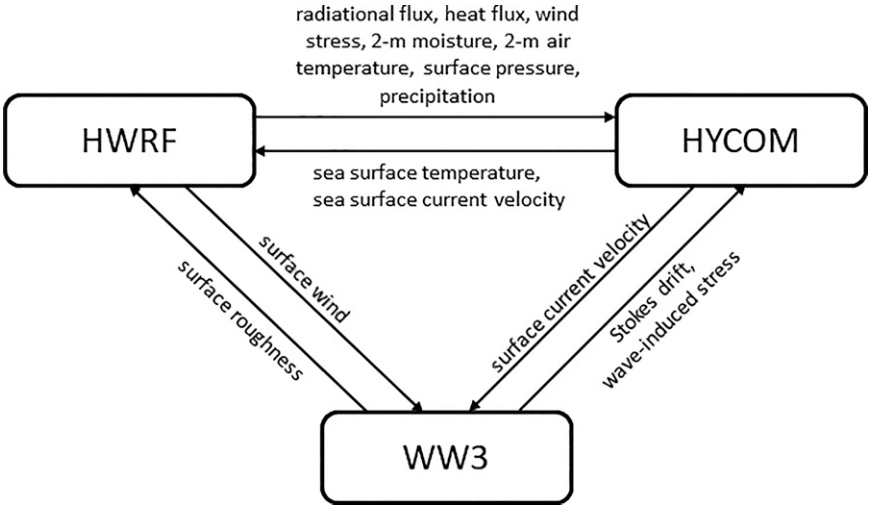

FIG. 1. Schematic of the HWRF system that shows the three-way coupling of the atmospheric model (HWRF), the ocean circulation model (HYCOM), and the surface wave model (WW3). Arrows denote the direction of data flow.

by the vortex relocation and the GSI-based data assimilation. The following cycles starts from a product of data assimilation using the 6-h forecasts from the previous cycle as the background. When tail Doppler radar observations are available the hybrid data assimilation with a 40-member ensemble Kalman filter (ENKF) is employed. More details are found in Biswas et al. (2018). The ocean component uses the RTOFS nowcasts and forecasts for ICs for the first cycle, through subset to the regional domain. For the following cycles, the ICs are the 6-h fields from the previous cycle ("warm start"). A similar subset approach is taken for the WW3 ICs from the NCEP global wave model forced by GFS, GFS-Wave. Although HYCOM employs closed BCs, HWRF updates the BCs at 6-h intervals with remapped GFS forecast products, and WW3 uses hourly GFS-Wave spectral forecasts.

The coupled system software is available at https://svn-dtc-hwrf.cgd.ucar.edu/trunk, and the scientific documentation and user's guide are available as well at https://dtcenter.org/community-code/hurricane-wrf-hwrf.

a. Atmospheric model

HWRF is a high-resolution, cloud-resolving regional model built on the Nonhydrostatic Mesoscale Model (NMM) dynamic core (Janjić et al. 2010) with a suite of physics specifically fine-tuned for TC forecasting applications (Gopalakrishnan et al. 2011; Biswas et al. 2018; Mehra et al. 2018). The dynamic solutions for the triple-nest configuration are sought at 13.5/4.5/1.5 km resolutions on an Earth-rotated Arakawa E-grid and 75 hybrid pressure-sigma vertical coordinates, with two-way feedback between the nesting and nest domains through up- and down-scaling,

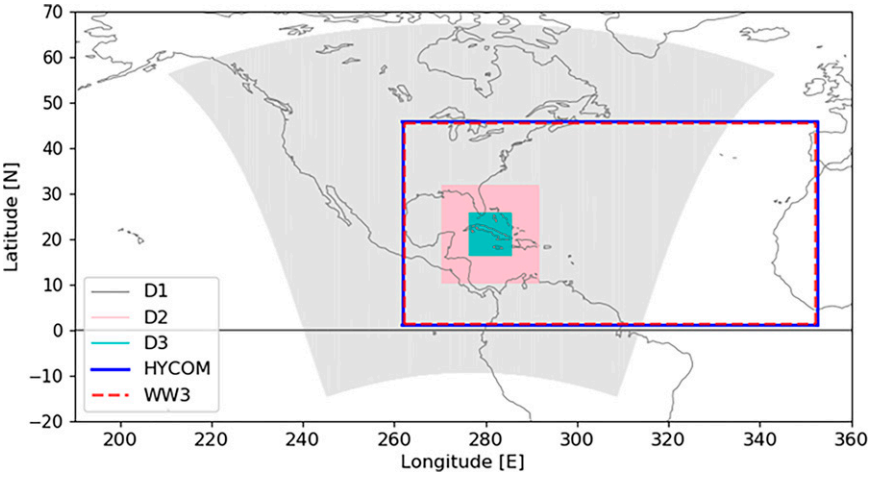

FIG. 2. The HWRF modeling area: the gray, pink, and cyan-shaded boxes denote the atmospheric outer (D1), intermediate (D2), and inner domains (D3), respectively. The blue rectangular box represents HYCOM, and the red dashed box denotes the WW3 domain.

except for six hourly updated boundary conditions for the outer domain.

The physics in HWRF is updated at once every third dynamic time step. The physics package includes Ferrier microphysics (Ferrier et al. 2002) for cloud processes, a rapid radiative transfer model (Iacono et al. 2008) for longwave and shortwave radiation, and a revised simplified Arakawa–Schubert convective scheme (Han and Pan 2011) for deep and shallow cumulus convection in the outer and intermediate domains. More details on the latest physics suites can be found in Biswas et al. (2018).

The planetary boundary layer (PBL) module estimates subgrid scale flux and provides the tendency of temperature, moisture, and momentum flux to the air column. Specifically, HWRF employs the nonlocal hybrid eddy-diffusivity mass-flux (hybrid EDMF) scheme to determine PBL height using the eddy diffusivity profile via iterating it until it matches the profile with the surface-layer fluxes from the ocean and land surface. Horizontal diffusion in the nest domains is parameterized with a flow-dependent length scale (Zhang and Marks 2015; Zhang et al. 2018; Wang et al. 2021). The PBL in HWRF is exclusively coupled to the surface slab model (Bender et al. 2007), where turbulent fluxes are estimated using the prescribed bulk exchange coefficients C_d and C_k for the momentum and heat flux. The coefficients C_d and C_k are defined as follows (Biswas et al. 2018):

$$C_d = k^2\left(\ln\frac{z_o}{z_l}\right)^{-2}, \quad \text{and} \tag{1}$$

$$C_k = k^2\left(\ln\frac{z_o}{z_l}\right)^{-1}\left(\ln\frac{z_o}{z_t}\right)^{-1}, \tag{2}$$

where κ is the von Kármán constant (0.4); z_o and z_t are the roughness length scales for the momentum and enthalpy flux, respectively; and z_l is the lowest model-level height. The 2020 version of HWRF employs fifth- and sixth-order polynomial functions of winds for z_o (appendix A) and z_t (appendix B), respectively, which are estimated by fitting them to historical field measurements under low and moderate winds and the wind tunnel laboratory results for high winds (see Biswas et al. 2018 for more details). The resultant exchange coefficients for the neutral conditions are shown in Figs. 4 and 3 in Biswas et al. (2018).

For ocean coupling, the outer and intermediate mesh grids use the SST feedback directly and the innermost domain uses up-scaled SSTs from the adjacent mesh grids to update the surface flux in the surface boundary layer using the bulk formulas (1) and (2). For three-way coupling, the atmospheric wind stress is estimated as follows, using relative winds ($\mathbf{U}_{10}$) to the sea surface current $\mathbf{u}_o$:

$$\tau_a = \rho_a C_d(\mathbf{U}_{10} - \mathbf{u}_o)|\mathbf{U}_{10} - \mathbf{u}_o|, \tag{3}$$

followed by subtracting the wave-induced stress (τ_w):

$$\tau_a = \rho_a C_d(\mathbf{U}_{10} - \mathbf{u}_o)|\mathbf{U}_{10} - \mathbf{u}_o| - \tau_w, \tag{4}$$

where ρ_a is the air density and C_d is the drag coefficient.

b. Oceanic model

HYCOM solves 3D governing hydrostatic primitive equations with no tides at 1/12° resolution on the Arakawa C grid and 41 hybrid z–σ vertical coordinates that follow depth coordinates at the surface and potential density surfaces in the interior (Bleck and Boudra 1981; Bleck 2002; Chassignet et al. 2003; Wallcraft et al. 2009). The regional HYCOM domain covers the North Atlantic basin from 261.8° to 352.5° in longitude and from 1.0° to 45.8° in latitude (Fig. 2). The initial and boundary conditions (IC/BCs) are subsets of the U.S. NCEP global RTOFS that has uncertainties of 0.68°C, 0.73°C, and 0.19 psu for T and S, respectively (Morrison et al. 2016; Ryan et al. 2015). Numerical procedures solving the governing equations, including the initial and boundary conditions (ICs/BCs), are referred to Kim et al. (2014). HYCOM employs the nonlocal K-profile parameterization scheme (KPP; Large et al. 1994; Halliwell 2004), which parameterizes turbulent momentum and scalar fluxes via diffusivity and viscosity profiles from the sea surface to the bottom of the boundary layer and nonlocal scalar fluxes in the layer.

There are different ways to exchange coupling parameters between the atmosphere and ocean circulation models. For instance, Benetazzo et al. (2013) and Hegermiller et al. (2019) have the ocean model component calculate turbulence heat flux and momentum flux using the Coupled Ocean-Atmosphere Response Experiment (COARE) v3.0 bulk flux algorithms which are valid for winds less than 20 m s^{-1} (Fairall et al. 2003). Our approach, instead, is to directly import atmospheric surface turbulent momentum flux [Eq. (3) or Eq. (4) for two-way and three-way coupling, respectively] and heat flux estimates using the length scale z_o and z_t, to force HYCOM (see Fig. 1).

When the three-way coupling is activated, HYCOM receives the depth- and frequency-integrated Stokes drift $\mathbf{U}_s$ (a monochromatic and deep-water surface gravity wave), the mean wavenumber K, and the wave-induced stress (τ_w) from the wave model, followed by projecting $\mathbf{U}_s$ to depth (z, downward), using the expression of $\mathbf{u}_s = \mathbf{U}_s e^{2Kz}$. HYCOM in turn updates the momentum [Eq. (4) in Ali et al. 2019], pressure gradient force, and continuity equations (Rogers and Wallcraft 2013), with Coriolis–Stokes forcing and the wind stress [Eq. (4)]

HYCOM's KPP mixing is enhanced by Langmuir turbulence to account for the wave-current-induced Langmuir circulation. There are four options of parameterization of the Langmuir mixing enhancement (F_l), which were referenced to (i) McWilliams and Sullivan (2000); (ii) Smyth et al. (2002); (iii) Harcourt and D'Asaro (2008); and (iv) Takaya et al. (2010). Preliminary results of sensitivity experiments for the cases of Hurricane Michael (2018) and Hurricane Laura (2020) suggest that options i, iii, and iv exhibit similar skills in their TC forecasts and also similar mixed layer depth (MLD) and SST cooling, whereas option ii results in poor intensity and track skill, compared to the other options. In this study, we used option i for the enhancement factor F_l expressed as $F_l = (1 + 0.080/L_a^4)^{1/2}$, where $L_a = (|\mathbf{u}^*|/|\mathbf{u}_s|)^{1/2}$ is the turbulent Langmuir number that measures the relative influence of

directly wind-driven shear (with frictional velocity $\mathbf{u}^*$) and the Stokes drift $\mathbf{U}_s$. Ali et al. (2019) reports from the study of intra-season and non-TC conditions that too much mixing with the option i. This is inconsistent with the results of the sensitivity study for TC Michael and Laura. Details from the sensitivity study for hurricane predictions to the alternative Langmuir mixing schemes will be explored in a follow-up study.

c. *Wave spectral model*

WW3 is version 6.05 of a third-generation model (Tolman 2014), with the source term (ST4) package (Ardhuin et al. 2010). Wind waves are described by the action of the density wave spectrum $S(K, \theta)$ (where K is the wavenumber and θ is the azimuthal angle) that is partitioned by 50 frequency bands ranging from 0.0350 to 0.9635 Hz with an incremental factor of 1.070 Hz and 36 evenly spaced directions starting at 5° from true North (°T).

The momentum exchange coefficient C_d is sensitive to shorter waves, i.e., the high-frequency wave spectrum. However, current wave models are unable to accurately represent the high-frequency part of the wind spectrum, due to parameterizations in unconstrained source terms in high-wind conditions. To estimate the full-wave spectrum, Moon et al. (2004a,b) employed the equilibrium tail model (Hara and Belcher 2002) for the under-resolved spectrum range higher than frequency $3f_{pi}$ and merged this with the wave spectrum simulated by WW3. To estimate z_o, they used the full spectrum and the mean wind profile determined by the assumption of the total stress τ_t ($= \tau_w + \tau_v$, where τ_w and τ_v are wave-induced and turbulence stress, respectively) and the bulk energy balance inside the wave boundary layer. The top and bottom boundaries are constrained by matching the τ_t to the atmospheric wind stress τ_a (typically a height of 10 m), and to the viscous stress τ_v (based on a roughness length scale z_v of $0.1K_v/\sqrt{\tau_v/\mu_a}$, where μ_a is the air viscosity, 1.45×10^{-5}), respectively (Moon et al. 2004a). In general, WW3 tail energies are overestimated. To mitigate, we estimate the saturation tail spectrum by assuming a linear transition in a range between $1.25f_{pi}$ and $3f_{pi}$, and a constant value at frequencies above $3f_{pi}$, as reported in R14. In this study, the precise value of the high-frequency spectral tail is determined as a function of the wind speed to produce a mean drag coefficient (over the various sea states) that is consistent with the bulk formula employed in the surface boundary layer in the atmosphere model. The form stress τ_w is estimated for a given wavenumber K at a height in the boundary layer ($z = \delta/K$, where δ is the height parameter and is set to 0.03) in the mean profile using the conservation of τ_t. The z_{ow} is calculated using

$$z_{ow} = z \exp\left(-\kappa \left|\frac{\mathbf{U}_c}{\mathbf{u}^*}\right|\right), \tag{5}$$

where κ is von Kármán's constant (0.4) and $|\mathbf{U}_c|$ is the wind speed at z corrected for its direction by the misalignment angle to account for the wind stress change due to crosswind swell (e.g., Porchetta et al. 2020; Holthuijsen et al. 2012; Hsu et al. 2017). The Charnock parameter $\alpha_w (= z_{ow}g/u^{*2})$ is diagnosed based on the resulting values of $\mathbf{u}^*$ and z_{ow} in Eq. (5). For the three-way coupling configuration in this study, WW3 passes the $\tilde{\alpha}$ ratio to the coupler:

$$\tilde{\alpha} = (z_{ow}g/u^{*2})/(z_o g/u^{*2}) = z_{ow}/z_o. \tag{6}$$

In turn, the surface boundary layer of the atmospheric model applies the $\tilde{\alpha}$ ratio after it is received from the coupler to update the momentum and enthalpy flux estimates using Eqs. (1) and (2), respectively.

3. Application

a. *Simulations*

To evaluate the impact of the fully coupled system on TC prediction (hereinafter H3W1), we also performed two-way HWRF-HYCOM coupling (H21H) and uncoupled HWRF forecasts (H21A), without tuning physics and parameterizations for the individual systems.

Each experiment was performed by covering the entire life cycle of Laura from 1800 UTC (20 August 2020) to 0600 UTC (27 August 2020), producing 27 verifiable cycles. Each cycle generated 126-h forecast products, including 3-hourly 1-min-sustained maximum wind (Vmax), minimum pressure (Pmin), TC center location, and the storm size for each storm quadrant for wind radii of 34 kt (R34), 50 kt (R50), 64 kt (R64), and the maximum wind (Rmax) as part of the postprocessing calculations (1 kt ≈ 0.51 m s^{-1}).

When an additional submodel is added, there is always a problem with balancing the mass, energy, and heat within the integrated model as a single unit. One option is tuning parameters, to minimize the imbalance and reduce the impact on the forwarded computation, or another approach is to employ a strongly coupled data assimilation. This study, however, uses none of them. It is because our objective of this study is to assess the TC forecast skill by adding a component model, but not the improvement of the three-way coupling system.

b. *Hurricane Laura 2020*

Hurricane Laura (13L) was one of nine TCs in 2020 that underwent rapid intensification (RI) for the season, becoming the first category-4 hurricane (peak 1-min sustained winds of 130 kt). The storm formed from a tropical wave south of the Cape Verde Islands on 17 August. For the next 48 h, the storm maintained its tropical depression (TD) status (green line in Fig. 3). At 1800 UTC 21 August, 12 h before traversing the Lesser Antilles, Laura became a tropical storm (TS), maintaining TS intensity as it passed over Cuba. As soon as Laura entered the Gulf of Mexico (GOM) at 0600 UTC 25 August the storm intensified into a category-1 hurricane. During the following 48 h, Laura traveled over relatively warm water in the northwest GOM, where it gained intensity gradually for the first 24 h, from 55 to 75 kt, and subsequently gained intensity exponentially up to 130 kt. At landfall in Cameron, Louisiana, United States, at 0600 UTC 27 August, Laura's maximum intensity was 130 kt, making it the strongest U.S. landfall TC in the 2020 season. It was reported that a 10-ft storm surge caused severe flooding along the Louisiana coast,

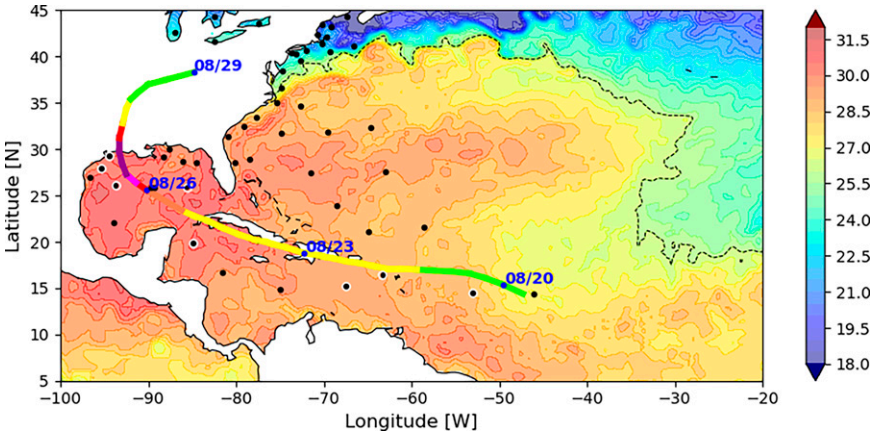

FIG. 3. Observed track and intensity of Hurricane Laura (13L) based on the Saffir–Simpson wind scale, superimposed on the optimum interpolation sea surface temperature (OISST) for 21 Aug 2020 (shaded) at 0.5°C intervals. Dashed curves represent 26°C SSTs. Black dots with and without white circles denote NDBC wave buoys (see Table 1) and temperature stations, respectively.

with at least 42 casualties and approximately USD $19 billion in damage.

Despite Laura's potential dissipation due to interaction with the land while traveling over the Lesser Antilles, the storm maintained its TS status, likely because of its relatively fast-moving speed (an average speed of 8 m s^{-1}) and the influence of the Bermuda high pressure system. After Laura left Cuba at 0600 UTC 25 August and was no longer influenced by Bermuda high, the storm entered a moisture-laden environment with weak shear due to a midlevel jet trough to the west. During Laura's northwestward transit over the GOM, the storm slowed from 7.5 to 6.5 m s^{-1} (~0000 UTC 27 August).

The main forecast assessment in this paper focuses on the period in which Laura traveled over the GOM. Pre-Laura oceanic conditions in the GOM consisted of mesoscale features that include cold-core water in the central gulf that separates the relatively warm GOM water into the western and eastern basins (Fig. 3). The loop current (LC) extended to ~26°N, with SSTs less than 32°C. Hurricane Marco passed over the central GOM between 22 and 25 August with 65 kt as its maximum intensity, and Laura crossed over the same area ~2 days later. Hence, this cold-core water (not clear in Fig. 3) might be partially influenced by Marco.

c. Observational data

Model validation was supported by observational data from the National Hurricane Center (NHC)'s best track (BT) database for TC center locations, intensity, and storm sizes; directional wave data from National Data Buoy Center (NDBC) buoys (black dots in Fig. 3) for significant wave height (Hs), peak period (Tp), and direction (D); and hydrographic profiles from a fleet of underwater gliders (Fig. 4) for model temperature (T) and salinity (S). Table 1 lists NDBC wave buoys selected within a 325-km distance from the observed TC locations (white open circles in Fig. 3, except for malfunctioning buoy 42001), including storm intensity and the approximate time of the storm.

Upper-ocean T and S observations were available from a fleet of gliders in two regions: the northern GOM (Fig. 4b) under the domain of the U.S. Integrated Ocean Observing System (IOOS) and in the vicinity of Puerto Rico (Fig. 4c), supported by the hurricane glider project of NOAA's Atlantic Oceanographic and Meteorological Laboratory (AOML). The T/S profiles were available at approximately 2-h intervals and to a depth of 900 m from all gliders, except Stommel and NG412 due to missing observations in the upper 25 m and instrument failure, respectively.

Evaluation of the domain-wide SST was conducted using a daily composite OISST Version 2 data record (Reynolds et al. 2007; Banzon et al. 2016). The products are available at 1/4° horizontal resolution and daily intervals from 1978 to the present.

4. Results

a. Atmospheric results

1) STORM TRACK AND INTENSITY

Figure 5 presents the results of homogeneous validations for 27 verifiable cycles from all experiments against the BT, showing that H3W1 and H21H improved track forecasts by 27% and 22%, respectively, compared to H21A (Fig. 5a). These improvements are statistically significant, particularly for the lead time of 96 h. A similar improvement, although not statistically significant, is found for the Vmax intensity (Fig. 5b), as indicated by reductions in the maximum mean absolute error (MAE) of ≤6.9 kt for H21A and ≤5.8 kt for H21H. Compared to H3W1, the relatively poor performance of H21H for track and intensity is not statistically significant at the 95% confidence interval, whereas the low forecasting performance of H21A is associated with large MAEs in terms

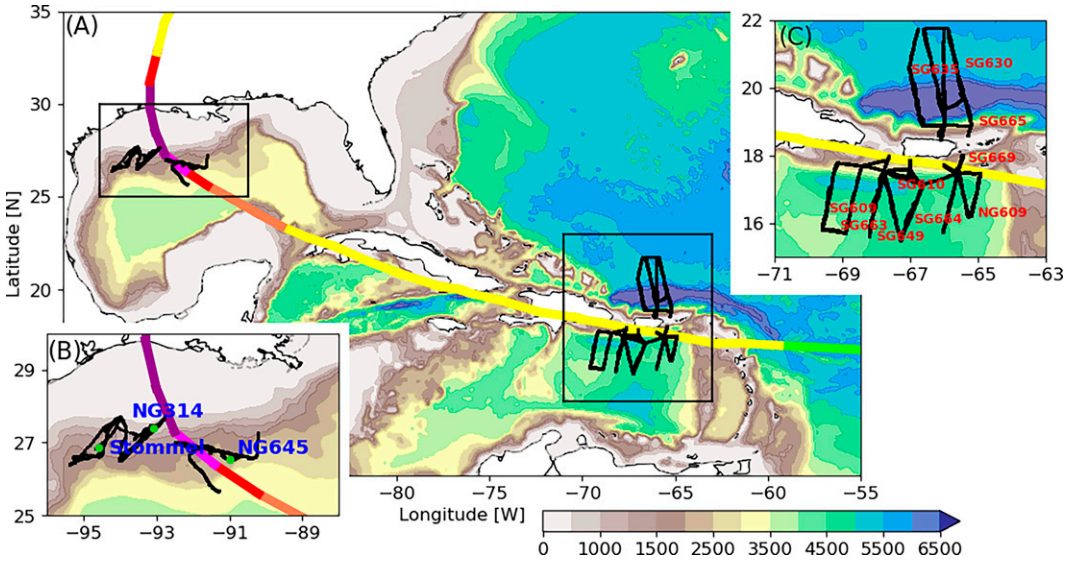

FIG. 4. (a)–(c) Glider sampling trajectories (black lines) superimposed Hurricane Laura's best track (Saffir–Simpson wind scale). Insets are enlarged areas of the rectangular boxes in (a), for a set of gliders in the northern Gulf of Mexico in (b), and in the vicinity of Puerto Rico in (c). Green dots along the glider tracks in (b) denote the locations at 0600 UTC 24 Aug 2020.

of both track (Fig. 5a) and intensity (Fig. 5b). For early cycles from 1800 UTC 20 August 2020 to 0600 UTC 22 August 2020, the track predictions are biased to the east of the BT (Fig. 6).

The track predictions for a total of 14 cycles after 1800 UTC 23 August 2020 agreed well with the BT and exhibited little bias, in contrast with the eastward bias for the previous 13 cycles (Fig. 6). The statistical results for all 27 cases indicate that the eastward bias (or rightward bias) is the worst for H21A and is less for H21H followed by H3W1. Similarly, the along track MAE and bias are the largest for H21A and the smallest for H3W1. For the early cycles, all the three models coincidently predict premature intensification. However, the H3W1 forecasts comparatively have less cases of false intensification (Figs. 6h,i) than H21A and H21H. It is also noted that the predicted intensity is generally higher for H21A, followed by H21H and then H3W1. Figure 6 clearly suggests better skills for the later cycle in both track and intensity than the earlier cycles. Among the late cycles, all three experiments produce comparable track prediction for the 0600 UTC 24 August 2020 cycle, which alleviates potential uncertainties. Hereafter, our analysis focuses on this cycle.

Comparisons of the track and intensity forecasts for the 0600 UTC 24 August 2020 cycle are presented in Fig. 7. It is noted that the predicted tracks are similar to the BT until 12 h before landfall, when H21A diverges westward, compared to H21H and H3W1 (Fig. 7a). All three experiments show early intensification. Among them, however, the H3W1 forecast agrees better with the BT in terms of RI magnitude, occurrence, and duration; and the H21A prediction is the worst, with the maximum intensity (149 kt) occurring ~12 h sooner and ~20 kt higher (Fig. 7b). The H21H forecast performance falls between H3W1 and H21A, showing a maximum intensity of 139 kt at 1800 UTC 26 August. The three experiments start intensification at 1800 UTC 24 August, 0600 UTC 25 August, and 0000 UTC 25 August for H21A, H21H, and H3W1, respectively, and reach a peak intensity of 149 kt at 0000 UTC 27 August for H21A, 139 kt at 1800 UTC 26 August for H21H, and 133 kt at 1800 UTC 26 August for H3W1. Hence,

TABLE 1. Directional wave NDBC buoys (black dots with white open circles in Fig. 4) within a 325-km distance from the Laura best track with negative (positive) means located at the west (east) of the best track.

ID	Longitude (°)	Latitude (°)	Distance (km)	UTC	Date	Pmin (hPa)	Vmax (kt)
42035	−94.413	29.232	−124	0600	27 Aug	938	130
42019	−95.345	27.910	−239	0000	27 Aug	938	130
42002	−93.646	26.055	−179	1800	26 Aug	952	120
42003	−85.615	25.925	277	1800	25 Aug	990	70
42056	−84.945	19.820	−324	0000	25 Aug	998	55
42059	−67.483	15.252	−295	1800	22 Aug	1004	45
42060	−63.331	16.433	−85	0000	22 Aug	1008	40
41040	−53.045	14.554	−231	1800	20 Aug	1008	30

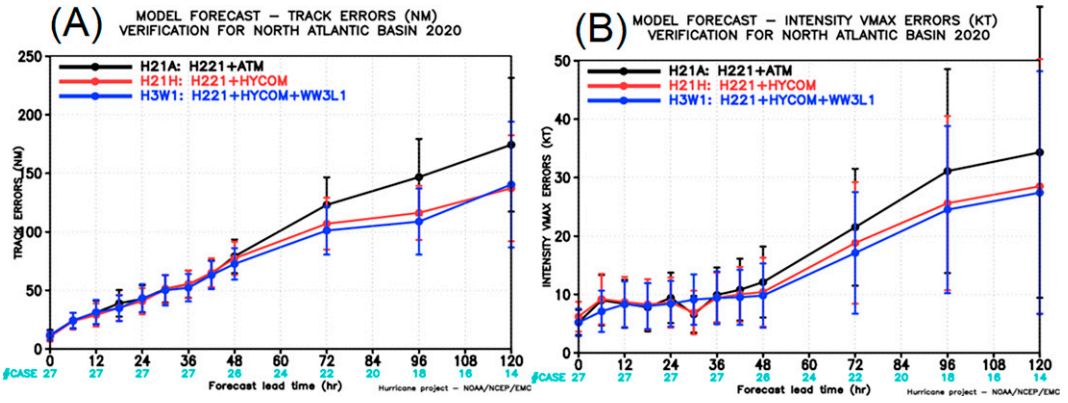

FIG. 5. Homogeneous comparisons of track and intensity forecasts showing the mean absolute error (MAE) for (a) the track and (b) minimum wind (Vmax) intensity, as a function of forecast lead time (h; in black) and the number of verified cases (in cyan). Vertical bars in (a) and (b) denote the 95% confidence intervals.

the RI magnitude for H3W1 is 78 kt (42 h)$^{-1}$, similar to the observed 80 kt (54 h)$^{-1}$ and with a lag of only 6 h.

2) STORM STRUCTURE

For simplicity, the analysis of the storm structure was based on the average of four-quadrant wind radii. The experiments showed a similar prediction of the radius of maximum wind (Rmax), with an MAE $\leq$ 20 n mi and a mean bias of -5 n mi (1 n mi = 1.852 km). Although not statistically significant, we noted that among the three runs the H21H Rmax variations were the highest, mainly in early lead time $\leq$ 30 h. An analysis of R34, R50, and R64 reveals the same characteristics between the experiments. First, the MAE magnitudes decreased with the increase in wind radii from ~30 n mi on average for R34 and ~20 n mi for R50 up to ~15 n mi for R64. Second, the bias predictions for R34 and R64 were similar to the observations, but all three runs predicted a negative bias by $O(18)$ n mi for R50. Overall, however, H3W1 forecast a smaller storm, compared to H21A and H21H.

Figure 8 shows Hovmöller diagrams of PBL height estimates as a function of the normalized radial distance (r) to Rmax (r/Rmax) in the x direction and the forecast lead time in the y direction. H21A (Fig. 8a) predicted the largest PBL height of ~2.5 km, as well as the largest spatial extent (5.4r/Rmax for 1.5-km height, for example), whereas H3W1 predicted (Fig. 8c) the lowest height (<2.2 km) and smallest radial extent (<4r/Rmax). A recent study that analyzed

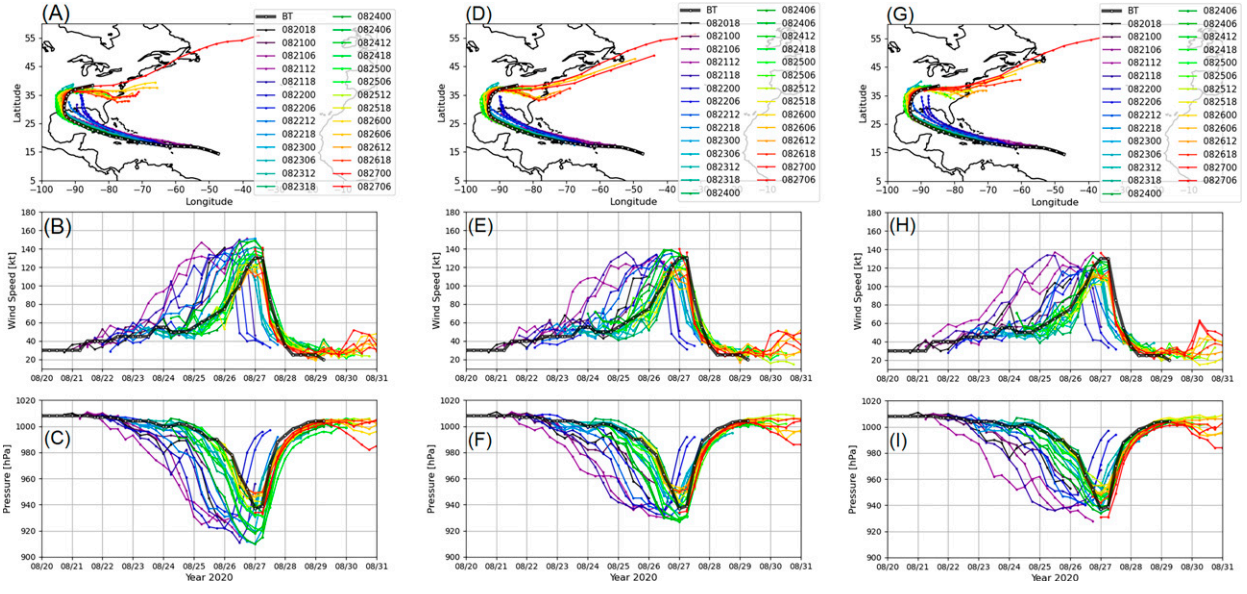

FIG. 6. (a),(d),(g) Track; (b),(e),(h) Vmax intensity; and (c),(f),(i) Pmin intensity forecast for the individual cycles (listed in the legend box in terms of month, day, and hour) for (left) H21A, (center) H21H, and (right) H3W1. The thick black lines with white dots are the observations (BT).

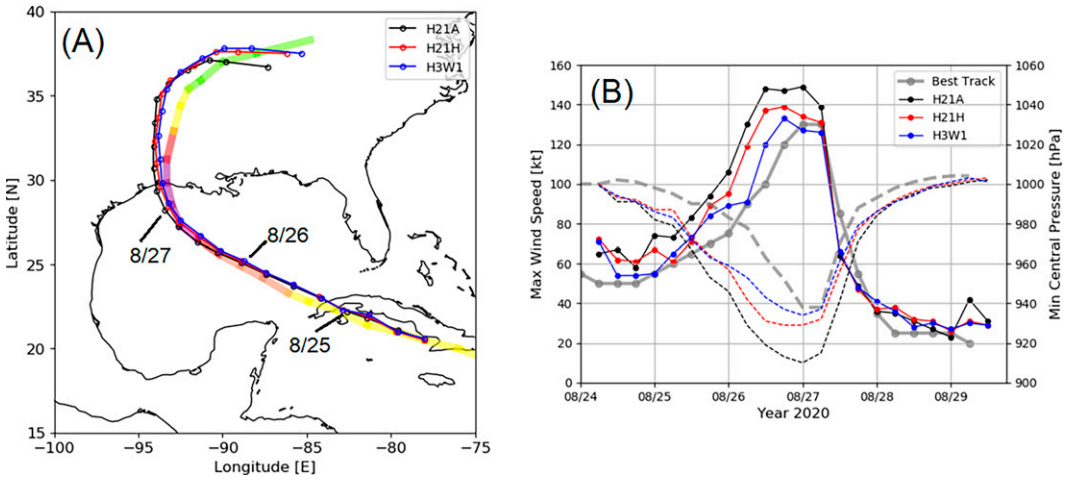

FIG. 7. (a) The 6-hourly track and (b) Vmax (solid)/Pmin (dashed) intensity forecasts for the 0600 UTC 24 Aug 2020 cycle: black, red, and blue lines in (a) and (b) denote uncoupling (H21A), two-way coupling (H21H), and three-way coupling (H3W1), respectively. The best track (BT) is shown in color in (a) based on the Saffir–Simpson wind scale and in gray in (b).

dropsonde data from 13 North Atlantic hurricanes from 1997 to 2005 (Zhang et al. 2011) reported that the inflow layer is different with different definitions of the PBL height, and that the mixed layer depth definition produces the highest height (1.5 km). Compared to the observations, HWRF generally predicts a higher PBL. Additional coupling (H3W1) appears to mitigate the overprediction by 12% (7%) and 4% (3%), reducing the H21A and H21H peak (mean) values, respectively. Zhang et al. (2015, 2018) reported that the relationship between PBL height and TC intensity is sensitive to vertical and horizontal mixing length scales. We followed this suggestion and employed the flow-dependent length scale demonstrated in Wang et al. (2021). There might be further tuning required for a fully coupled model, but lowering the overestimated height via uncoupling and two-way coupling is evident. This is probably explained by the reduction in turbulent momentum flux (an example is shown in Figs. 9a–c) and heat flux (as shown in Figs. 20a–c).

3) WIND STRESS

Wind stress τ_a was computed from the HWRF surface layer scheme with the option of direct communication with HYCOM for surface ocean currents $\mathbf{u}_o$ as well as the ASIM for wave stress τ_t and roughness z_{ow}. Figures 9a–c show the 54-h forecast wind stress for the 0600 UTC 24 August 2020 cycle. H21A predicted an axisymmetric pattern with a maximum value of 10.0 N m^{-2} in the TC eyewall (Fig. 9a). For comparison, H21H (Fig. 9b) and H3W1 (Fig. 9c) were weaker and more asymmetric toward the right side, with peak values of 8.8 and 6.8 N m^{-2}.

Figures 9d–f show the instantaneous C_d corresponding to the wind stress (Figs. 9a–c). There were significant differences between H21A and H3W1. For instance, a high C_d (0.0026) value for H21A can be observed in the front right quadrants, extending from R64 to R50 and from the front to the rear quadrants (Fig. 9d). Conversely, the same C_d is found in the rear right quadrant for H3W1 (Fig. 9f). This suggests that a large reduction takes place between the front and rear sides in the right quadrant through the full coupling. Meanwhile, the H21H C_d field (Fig. 9e) is similar to the H3W1 counterpart of a concentric pattern, except for the magnitudes.

Figure 10a shows the estimates of the Charnock coefficient ratio, $\tilde{\alpha}$ [Eq. (6)], depicted in the zoomed-in inset area in Fig. 8f. In general, $\tilde{\alpha}$ is less than 1 and the small value is observed in the right quadrant along the Rmax (red dashed line), ranging from the minimum of 0.2 to 0.6. This is in agreement with Moon et al. (2004b), who reported small z_{ow} values in high winds caused by young seas aligned with local winds, and supports the reduction of C_d with wind speed. Figures 10b–d show C_d for each quadrant, as a function of 10-m wind for each experiment. Notable impact by the three-way coupling is found in low winds below ~10 m s^{-1}, showing large variations in the northwest (NW) quadrant, followed by the southwest (SW), northeast (NE), and southeast (SE) quadrant (Fig. 10b). A similar finding exists for the H21H C_d (Fig. 10c), except the shift of a local minimum wind. Apparently, the H21A C_d follows the predescribed curve the most (Fig. 10d). In conclusion, the momentum flux is sensitive to $\tilde{\alpha}$, and its spatial variability alters the τ_a field, not C_d. Only quadrant-dependent C_d exists in a low wind regime. Hence, the direct use of sea-state-dependent roughness length scale is recommended in place of the pre-described functions for z_o (appendix A).

b. *Ocean results*

1) SEA SURFACE TEMPERATURE

The daily composite 1/4° OISST shown in Fig. 11a demonstrates that significant SST cooling occurred for 7 days (21–17 August 2020) in the GOM. This cooling varied on a spatial scale of 100 km. The local peak in cooling was 2.5°C at ~25.5°N, 87.5°W , followed by a second peak of 2.0°C at

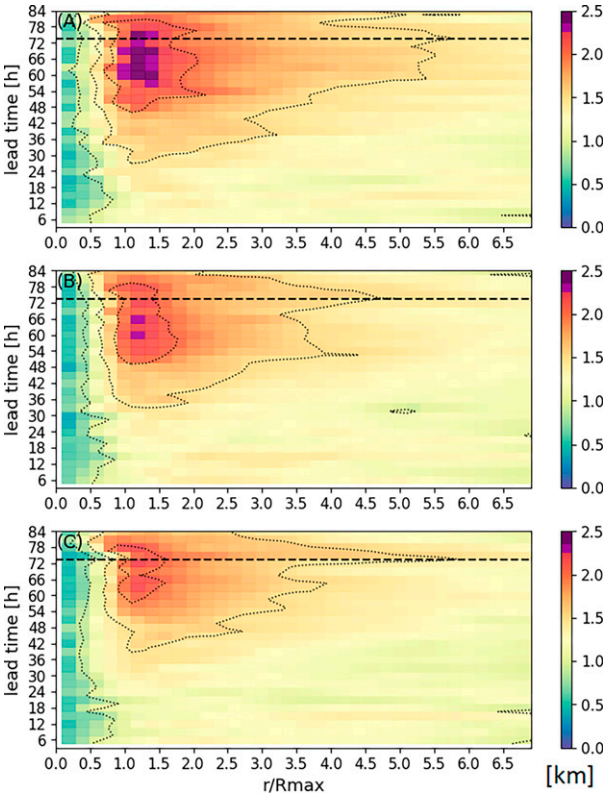

FIG. 8. Height prediction of the planetary boundary layer (km) per unit-normalized radial distance (r/Rmax) for (a) H21A, (b) H21H, and (c) H3W1, with lead times from 3 to 78 h for the 0600 UTC 24 August 2020 cycle (y axis). Dashed contours denote heights of 1.0, 1.5, and 2.0 km, for reference. The horizontal dashed line represents landfall.

26.8°N, 90.5°W. Both extremes are located ~37 km east of the BT. An asymmetric pattern can be observed between the western and eastern GOM. This may be the result of the compound impact of Laura and Marco, of which the paths crossed ~24°N, 87°W ~2 days apart with a maximum sustained wind of 65 kt for both.

Figure 11b shows the daily SST difference from day 0 (21 August) estimated along the track ~30 km east (dots in Fig. 11a) of the BT. Low day-0 SSTs cover the area east of the Lesser Antilles (see Fig. 3), where the maximum cooling $O(1)$°C is found at day 4 (light blue) in an area around the West Indies. SST becomes warmer thereafter. These warm SSTs in the GOM (shaded box in Fig. 11b) are already cooler by day 1 and continue to cool with time (red dots). This suggests that the area had already been influenced by Hurricane Marco from day 1. The SST cooling in GOM is further increased by Laura with time, showing $O(0.8)$°C at day 3 to ~2.5°C at day 6.

To estimate the model SSTs for comparisons with the daily analysis, we used the predicted track for the 0600 UTC 24 August 2020 cycle run to find locations ~37 km east. To produce daily model SST estimates, we first made a temporal average of 24 consecutive hourly outputs, followed by mapping the 1/12° resolution to the OISST grid spacing (1/4°). The results (Fig. 12) demonstrate that H21H and H3W1 both underpredict SSTs compared to the composite product. This negative bias gradually increased with time, with peak values as large as 0.8° and 1.0°C at day 5 for H21H and H3W1, respectively. Considering the uncertainties propagated through interpolating and averaging, i.e., $O(1.25)$°C and $O(0.90)$°C for H21H and H3W1, respectively, and the OISST error of $O(0.83)$°C, the differences from the analysis products were not statistically significant. Nevertheless, the H3W1 SST was consistently cooler than the H21H by an average of 0.25°–0.30°C.

2) UPPER LAYER

Simulations were compared to the glider observations using a set of metrics of near-surface (10-m depth) temperature (Temp) and salinity (Salt), mixed-layer depth/temperature/salinity (MLD/MLT/MLS), ocean heat content (OHC), and mean temperature in the upper 100 m (T100). Figure 13 presents the statistics in normalized Taylor skill diagrams H21H (red) and H3W1 (blue) for the pre-storm cycle 0000 UTC 21 August 2020 (Fig. 13a) and the intensification cycle 0600 UTC 24 August 2020 (Fig. 13b). For the pre-storm case, the predictability for all variables was similar between H21H and H3W1, except for MLT (upper triangle), in which H21H (red) gave better predictions than H3W1 (blue). Among the metrics, Temp (represented by diamonds) demonstrated the best performance for H21H and H3W1, having a correlation coefficient (R) of 0.99, a standard deviation (STD) of 0.96, and a centered root-mean-square error (CRMSE) of ~0.10, followed by Salt (circles) with ~0.95 R, $O(0.9)$ STD, and ~0.40 CRMSE. MLD (stars) exhibited the worst performance. The OHC simulation was also in the lower skill range, showing a relatively small R of $O(0.65)$, large STD, and a CRMSE of ~1.30 and ~1.05, respectively, for H21H and H3W1.

For the TC intensification period (Fig. 13b), the performance of Temp and Salt remained high for both H3W1 and H21H, with values of ~0.99 R, 0.90 STD, 0.10 CRMSE and 0.92–0.95 R, 0.8–0.9 STD, 0.25–0.30 CRMSE, respectively. However, the H3W1 OHC (squares) and T100 (pluses) outperformed H21H. For the integrated variable MLT, H3W1 maintained its pre-storm performance, but the performance of H21H declined, compared to the pre-storm case. The MLS performance of H3W1 and H21H MLS improved for the intensification case but, compared with each other, their performance was reversed, with H21H performing better than H3W1. The MLD performance of both H3W1 and H21H was degraded for the in-storm case, showing a low R of 0.15–0.2, a low STD (0.1), and a CRMSE of ~0.50. The low STD and CRMSE imply little variation in the MLD, which might be the case since the upper ocean response to the storm was overwhelmed by data from a remote area, i.e., samples collected in the vicinity of Puerto Rico.

A close examination of the upper ocean's response to Laura for the intensification case was conducted using observations from glider NG645. Glider NG645 encountered Laura near the final stage of intensification. Figure 14 shows model T (left panels) and S transections (right panels), sampled

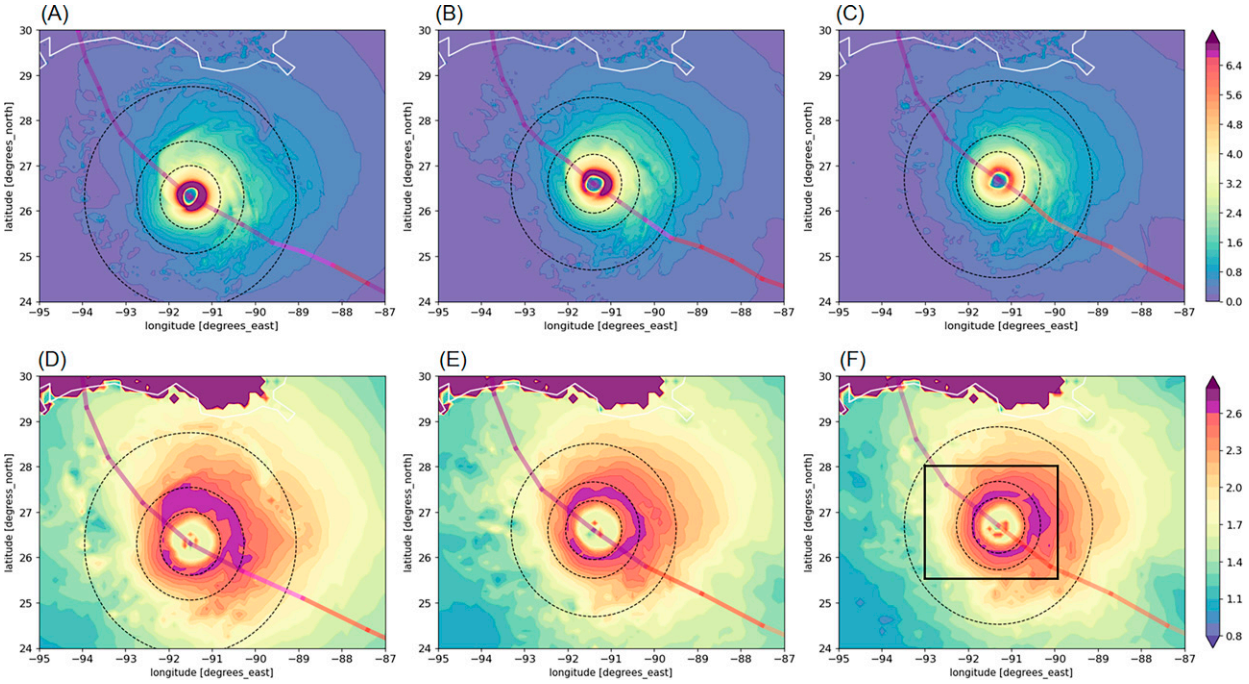

FIG. 9. The 54-h forecast for (top) wind stress and (bottom) drag coefficient C_d simulations for (a),(d) H21A; (b),(e) H21H; and (c),(f) H3W1, superimposed on the predicted track based on the Saffir–Simpson wind scale. Dashed circles denote the radius of predicted 34-, 50-, and 64-kt wind. The solid box in (f) is referred to in Fig. 10a.

following the glider observations (Figs. 14a,b) for the period from 0600 UTC 24 August to 1200 UTC 29 August. The observed pre-storm MLD and Z26 were centered at ~22 and ~80 m, respectively, with little variation, but the storm-excited upwelling and mixing resulted in the undulation and shoaling of MLD and Z26 for the post-storm period. A similar variation was predicted for H21H and H3W1 before and after the storm, except the H3W1 MLD and Z26 values were shallower by an average of ~15 and ~20 m, respectively, than their H21H counterparts. It can be noted, however, that the H3W1 MLD value was in better agreement with the observed value. The storm-induced cooling in MLD at NG645 was ~0.8°C, and the model produced cooling values of 0.6° and 1.3°C for H21H and H3W1, respectively. The observed S values varied from 35.4 to 36.7 psu, with an average of 36.1 psu. There was good agreement between the observations and the S values of H21H, with a mean difference (MD) of −0.36 psu and a CRMSE of 0.67. Conversely, the S value of H3W1 was less salty on average (MD of −0.27 psu) and varied close to the observation (RMSE of 0.59 psu). The CRMSE for H21H accounted for the relatively uniform S values in the upper 180 m. In contrast, H3W1 exhibited similar variations in depth, as well as in time, as the observed results, with a minimum S of 33.0 psu on 25 August in the near-surface layer (Fig. 13f). This freshwater is advected from the northeast (not shown) and is dissipated through wind mixing.

The upper ocean's response, observed by glider NG314 west of the storm track, was less dramatic. The MD values of H21H T for the pre and in-storm period were 0.6° and 0.5°C, respectively, and 0.7°C before and 0.9°C for H3W1, respectively. Conversely, the model's S value was quite similar to the observed one for both the storm periods, with an MD in the range of 0.01–0.03 psu and an RMSE of 0.15–0.17 psu. The differences from the observations are slightly beyond or within the HYCOM uncertainties (Morrison et al. 2016; Ryan et al. 2015).

3) SST COOLING

In section 4b(1), we discussed SST comparisons but at a coarse and daily resolution. In this section, we investigate SSTs at shorter temporal and smaller spatial scales. Due to the unavailability of products higher than the daily frequency, relative comparisons were conducted among the three experiments. We chose the TC footprint, defined by an area inside a radius of 500 km from the TC center. Figure 15 shows the 42- and 54-h SST forecasts for H21A (Figs. 15a,d), H21H (Figs. 15b,e), and H3W1 (Figs. 15c,f). One can immediately note the lack of storm-induced cooling for H21A (Figs. 14a and 15d). Although H21H and H3W1 predicted cooling at 2.4° and 2.9°C, respectively, the 42 h cooling for the latter (Fig. 15c) was higher than the former (Fig. 15b), by $O(0.5)$°C at R50 in the rear-right quadrant, for instance. The difference in SST in the rear-right quadrant beyond R50 for both the runs was cooler by $O(0.5)$°C than the magnitude at the inner radius (R50), and this was primarily due to vertical entrainment (Brand 1971; Shay et al. 1992, 2000; Shay and Uhlhorn 2008). In that area especially, cold water between the LC and a warm eddy was further enhanced by Laura, more so for H3W1. A local maximum vertical velocity was predicted, centered at ~80 m, with a magnitude of 0.20 and 0.22 cm^{-1} for

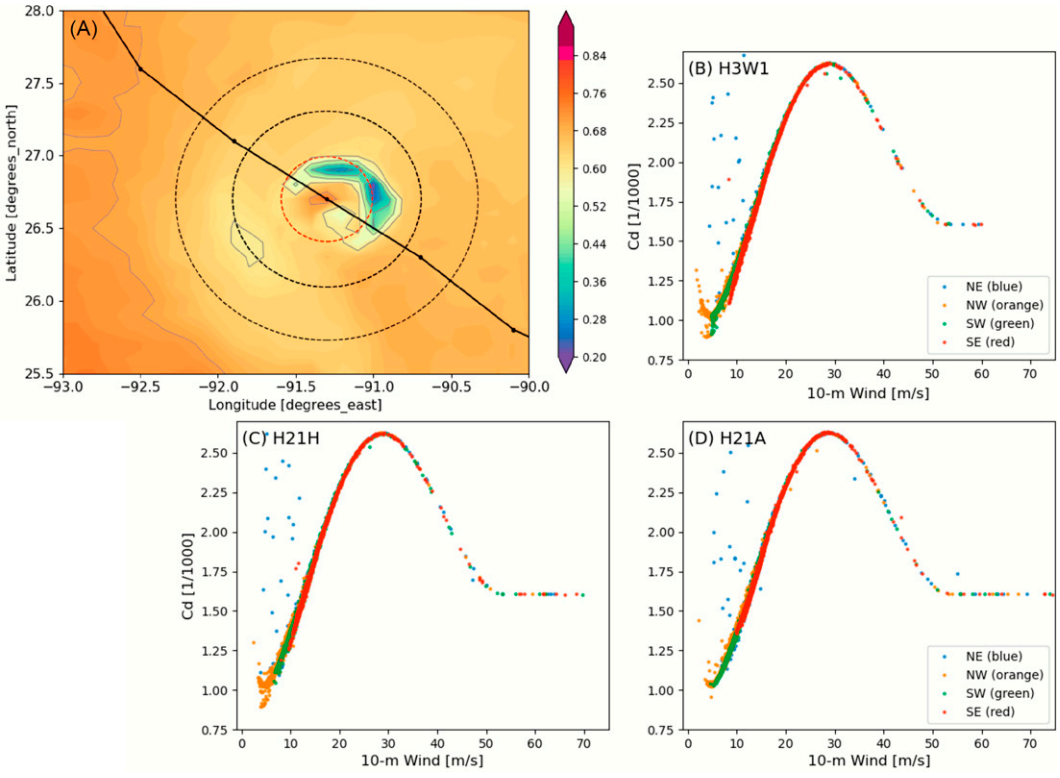

FIG. 10. (a) The 54-h forecast for the Charnock coefficient ratio [shaded at 0.1 contour intervals in (a)] and the drag coefficient C_d as a function of predicted winds each quadrant for (b) H3W1, (c) H21H, and (d) H21A. Data shown are from the 0600 UTC 24 August 2020 cycle simulations. Black and red contours in (a) denote the radius of the wind threshold of 50 kt (inner) and 64 kt (outer), and the maximum wind (Rmax), respectively. Blue, orange, green, and red dots in (b)–(d) represent the C_d estimates for the northeast (NE), northwest (NW), southwest (SW), and southeast (SE) quadrant, respectively.

H21H and H3W1, respectively. Hence, the upwelling was not a major driving force. A similar cold-water enhancement was observed during Katrina and Rita in 2005 by Jaimes and Shay (2009). The magnitude of the observed cooling for Rita in GOM was greater than 4°C, and it was explained by wind-driven upwelling at a magnitude of 1 cm^{-1} (Jaimes and Shay 2009). Our estimates of SST cooling and vertical velocity in this study are approximately 50% smaller than those of their study. This can be explained by the TC intensity differences between category-2 Laura and category-4 Katrina and Rita.

At 54 h at 1200 UTC 26 August (Figs. 15d,e,f), the storm was located in the warm northern GOM, with a temperature above 30°C. The persistent SST for H21A (Fig. 15d) accounts for this prediction of high intensity (148 kt). Despite the 17-kt intensity difference between H21H (137 kt) and H3W1 (120 kt), the

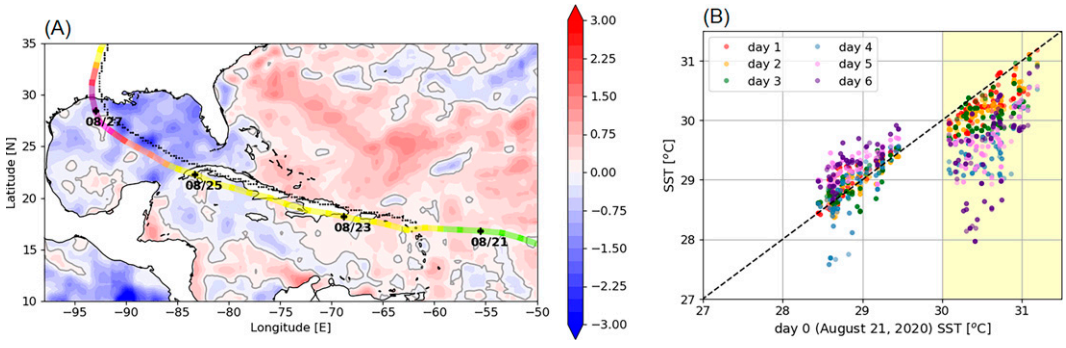

FIG. 11. (a) Daily OISST estimates of SST cooling in the GOM for 21–27 Aug 2020, and (b) SSTs at different locations [black dots in (a) sampled each day from day 0 (21 Aug 2020)] ~37 km east of the best track.

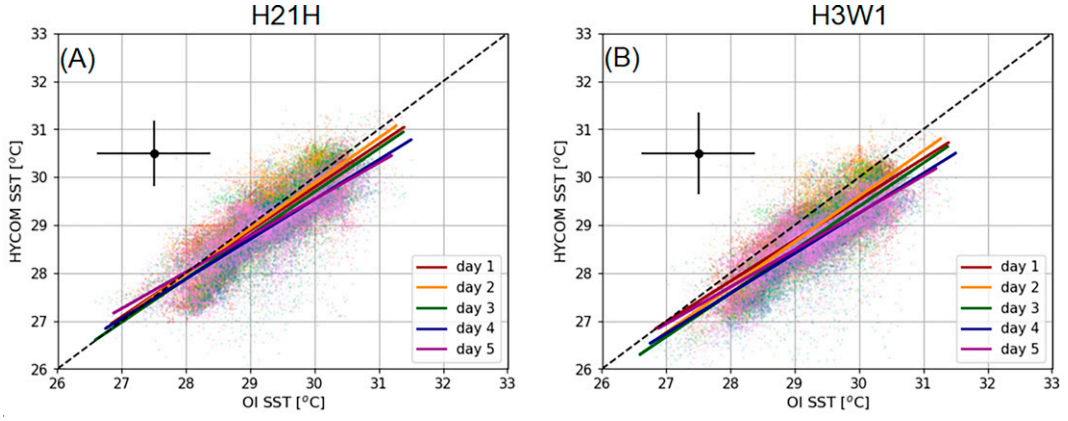

FIG. 12. Comparisons of the model's daily averaged SST (y axis) and OISST (x axis) for the 0600 UTC 24 Aug 2020 cycle, with error bars associated with the estimates in (a) the two-way coupled run (H21H) and (b) the three-way coupled run (H3W1). The area considered spans from 260° to 335°E in longitude and from 5° to 40°N in latitude.

H3W1 SST prediction inside R34 was about 0.5°C cooler than that of H21H.

c. *Wave results*

We validated significant wave height (Hs) and peak period (Tp) forecasts using directional wave observations from 34 NDBC buoy stations in the western North Atlantic basin (Fig. 4). Among these, we chose two stations: one to the east (buoy 42003) and the other to the west (buoy 42019) of the track. Figure 16 shows the results based on the 0600 UTC 24 August 2020 cycle simulations in a normalized Taylor diagram. A comparison of observations from the 34 stations suggests that H3W1 had a higher overall performance for Hs (red diamond), with 0.90 R, 1.10 STD, and 0.45 CRMSE, and comparatively lower performance for Tp (blue circle), having 0.53 R, 0.95 STD, and 0.90 CRMSE. The Hs performance is related to prediction skills of the 10-m wind speed (u10; green triangle) and wind direction (udir; yellow reverse triangle). The low Tp statistics were probably dominated by discrepancies from the stations in a remote area.

Direct comparisons of predicted wave properties were made at two NDBC stations, 42003 and 42019, using the time series of plots for five days from 0600 UTC 24 August to 1200 UTC 29 August 2020 (Fig. 17). The predicted and observed Hs values showed good agreement, with a correlation coefficient of 0.96, with peak values of 6 and 4 m for the east (42003) and west stations (42019), respectively. The Tp predictions also showed good agreement with the observations,

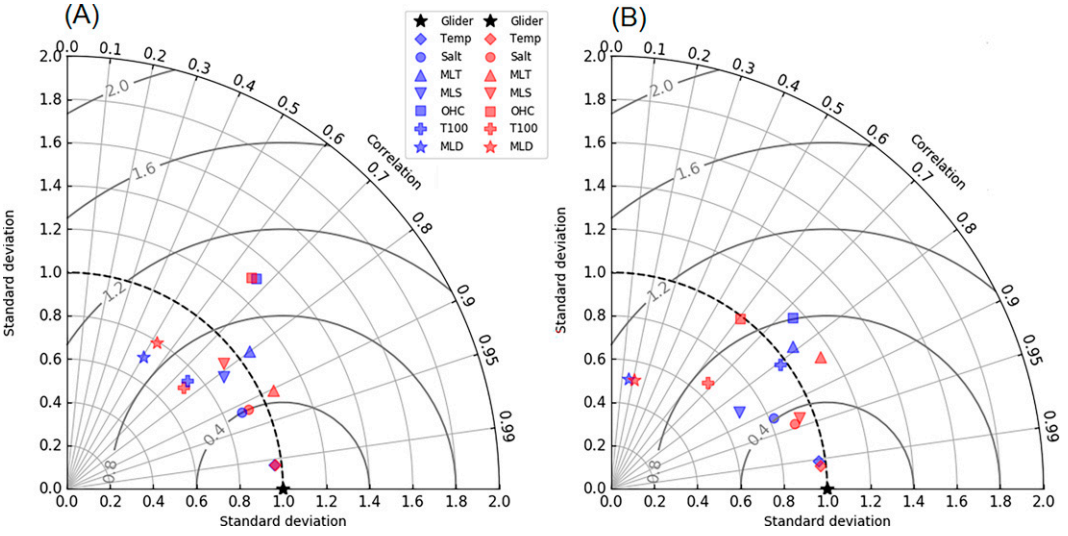

FIG. 13. Representation of the performance of ocean variables for the H3W1 (blue) and H21H (red) simulations, compared to observations (black star), in normalized Taylor diagrams with the standard deviation on the radial axis, the correlation coefficient on the angular axis, and the centered root-mean-square error (CRMSE) for solid thick curves: (a) the 0000 UTC 21 Aug 2020 cycle and (b) the 0600 UTC 24 Aug 2020 cycle. The observations were obtained from 13 gliders in the Gulf of Mexico and the vicinity of Puerto Rico.

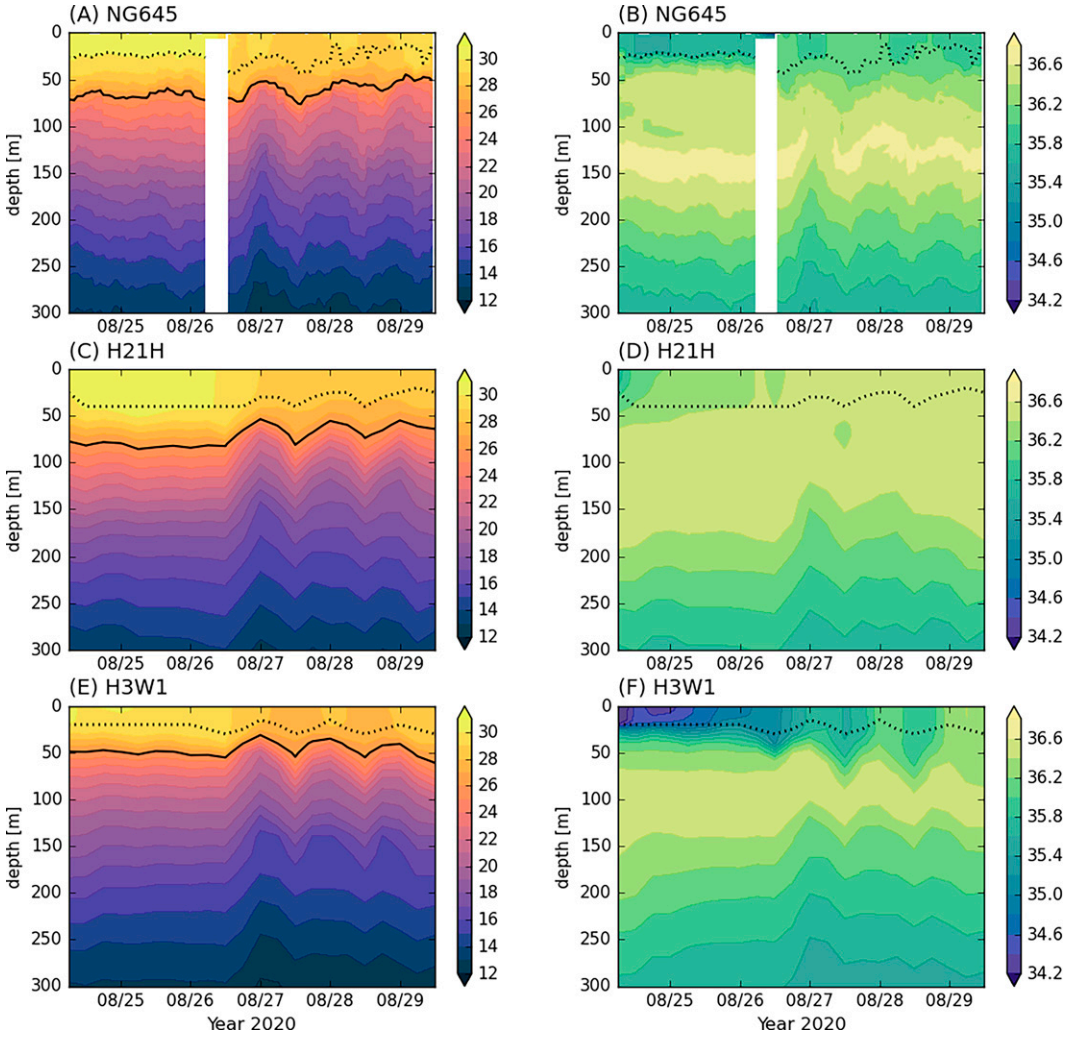

FIG. 14. Comparisons of (a),(c),(e) temperature and (b),(d),(f) salinity transects between glider (top) NG645 track, (middle) H21H, and (bottom) H3W1 data, from 0600 UTC 24 Aug to 1200 UTC 29 Aug (y axis). The simulations involved the forecasts for the 0600 UTC 24 Aug 2020 cycle, and they were interpolated to the glider transect. The dotted contour denotes MLD, and the solid contours represent the depth of the 26°C isotherm (Z26).

but their correlation coefficients were smaller, i.e., 0.78 and 0.80, respectively, likely due to lagging, primarily for the period of the storm approaching between 0600 and 1800 UTC August, with the predicted wind speed ranging from 10.9 to 14.2 m s^{-1} (Fig. 17c). Potential sources to explain this discrepancy include the prediction track and intensity errors of ~55.0 km and 9.0 kt over the 12 h, respectively. During this period, wave predictions that changed from dominant waves combined with individual waves to single-wind seas may account for the differences evident in Figs. 17a and 17b.

Station 42019 recorded the maximum Hs of 4.5 m at 2100 UTC 26 August. H3W1 predicted 4.1 m Hs (Fig. 16e), suggesting that this was not exactly wind seas but combined wind waves and swells generated by the TC located ~249 km to the east.

We found that storm-induced waves not only influenced the field near the TC but also had an impact ahead of the storm (mostly due to swell) that was evident at the 42019 station. This is particularly important when a storm approaches the coast. The model wave height grows tall in open water in parallel with the wind increase, having higher, longer, older, and growing waves on the right side of the TC. The maximum Hs (~13.5 m at 54 h) was typically located in the right quadrant. However, with the increase in time the long waves extended from the storm's front-right quadrant to the front right and left quadrants, concurrently growing longer from $O(120)$ m at 24 h (valid at 0600 UTC 26 August 2020) to $O(300)$ m at 54 h (valid at 1200 UTC 26 August 2020), for example. Coincidentally, after forecast hour 54, H3W1 predicted forerunner waves running in parallel with the coastline, more conspicuous on the west of the predicted track, in contrast to the asymmetric wave field when the storm is on the open ocean. This implies that waves become fetch-limited as a storm approaches the coastline, and they are reflected.

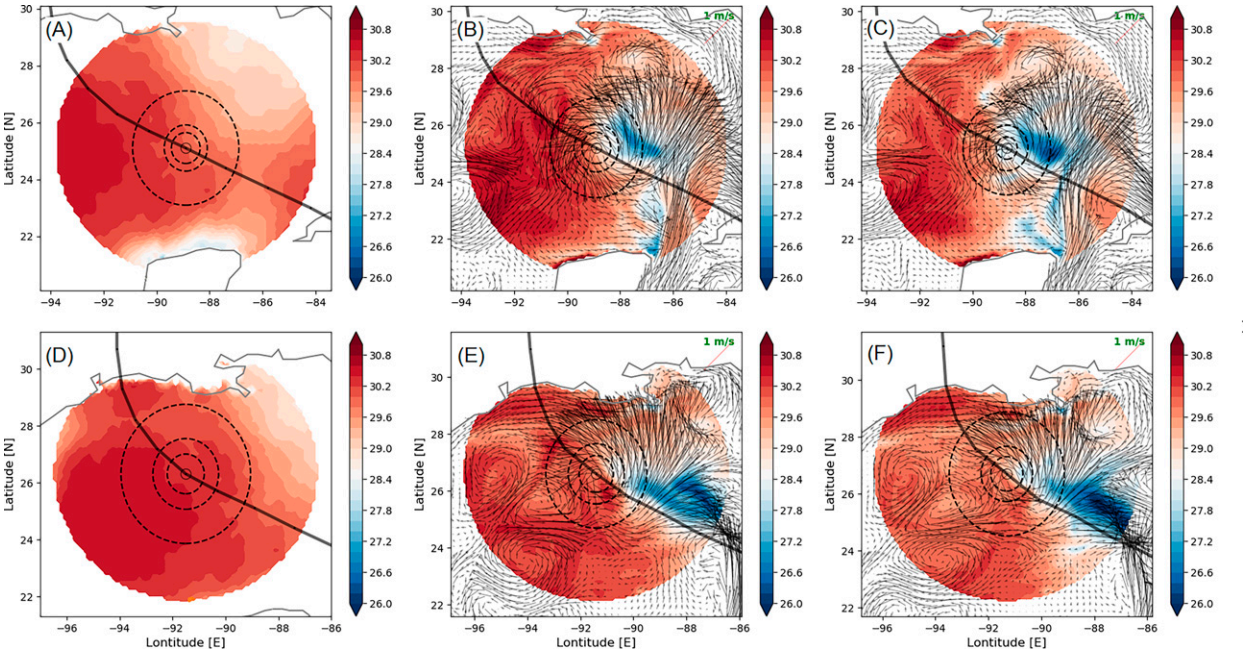

FIG. 15. Set of (top) 42-h and bottom) 54-h forecast SSTs for a footprint (500-km radius from the TC center) from the 0600 UTC 24 Aug 2020 cycle for (a),(d) H21A; (b),(e) H21H; and (c),(f) H3W1. Black arrows in (b) and (c) and (e) and (f) indicate the forecast surface currents. The black line denotes the predicted track. Dashed circles represent the predicted radius of the 34-kt (R34), 50-kt (R50), and 64-kt (R64) winds.

An additional feature in the GOM is a wave setup from a previous storm that can influence the wave height prediction for the following TC. For example, buoys 42003, 42039, 42002, and 42019 showed Hs values greater than at least 1 m after Marco and before Laura. Another example is a similar wave setup for a slow-moving or recurving TC, e.g., Isidore (2002), which exhibited Hs values greater than 2 m and less than 5 m for about 5 days at NDBC buoys 42040, 42002, and 42019 (Chao et al. 2005). This suggests the complexity of the upper ocean response to a TC in GOM, and wave coupling should be considered in numerical studies.

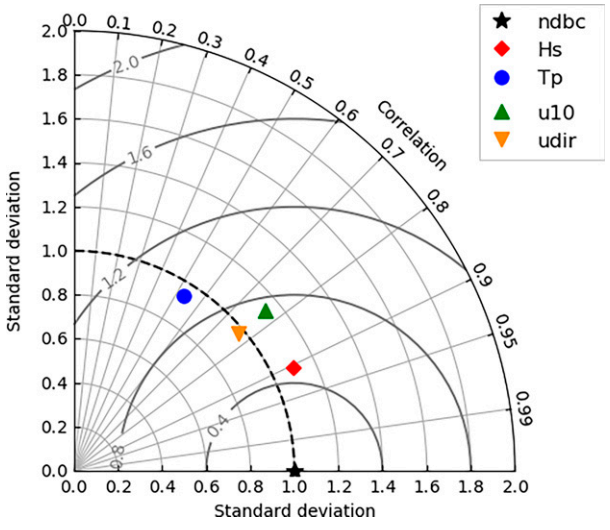

FIG. 16. Normalized Taylor diagram for significant wave height (Hs), peak period (Tp), 10-m wind (u10), and 10-m wind direction (udir) between the model and NDBC observations (NDBC) for the 0600 UTC 24 Aug 2020 cycle.

d. Ocean heat content (OHC)

To investigate the OHC response to Laura, we estimated OHC using the definition provided in Leipper and Volgenau (1972):

$$\mathrm{OHC} = \int_{z_{26}}^{0} \rho_w C_p (T - 26)\delta z,$$

where ρ_w is the seawater density, C_p is the specific heat capacity at constant pressure, T is the seawater temperature (°C), z is the depth, and z_{26} is the depth of the 26°C isotherm. The initial OHC is similar between H21H (Fig. 18a) and H3W1 (Fig. 18b), including the locations of the maximum OHC (197 kJ cm^{-2} for H21H and 189 kJ cm^{-2} for H3W1) in the Colombia basin, the high OHC (145 kJ cm^{-2}) at the LC, and the low OHC of ~25 kJ cm^{-2} between a warm eddy and the LC. Over 60 forecast hours, OHC changes are substantial, having a local maximum in the east or behind the TC center with the maximum of 68 kJ cm^{-2} recorded for H21H (Fig. 18c) and 48 kJ cm^{-2} for H3W1 (Fig. 18d). Another notable difference is that the H21H OHC loss extends farther to the east than the H3W1. This is probably due to the intensity and TC size predictions. Compared to H3W1, the average

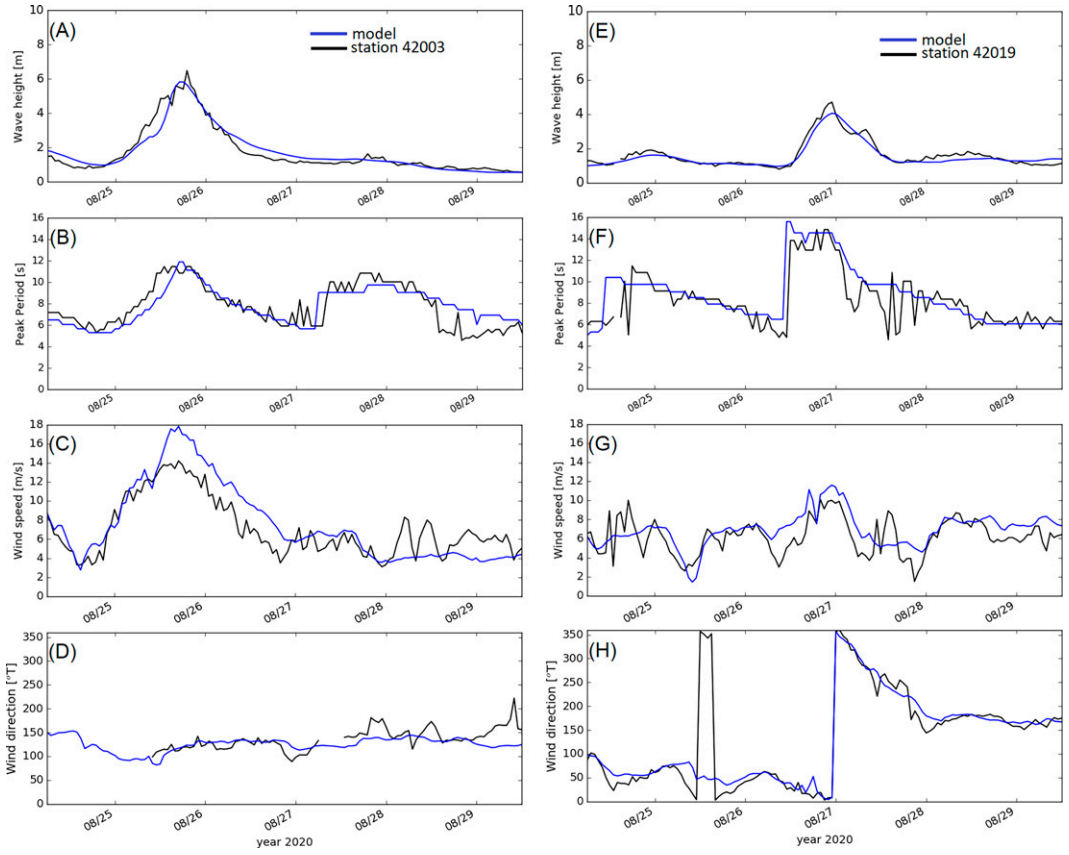

FIG. 17. Comparisons of a time series of (a),(e) significant wave height (m); (b),(f) peak period (s), (c),(g) 10-m wind (m s^{-1}); and (d),(h) 10-m wind direction from true north between H3W1 simulations (blue) and observations (black) at stations (left) 42003 and (right) 42019.

Vmax and R34 for 60 h are 7.8 kt higher and 16.35 km larger, respectively.

Comparing the model's OHC values to the observations, the loss due to Laura was more apparent at NG645 than NG314 (Figs. 19a,c). At NG645, the observed OHC loss was ~32 kJ cm^{-2} (Fig. 19a) from ~85 to 53 kJ cm^{-2} on average before and after Laura, respectively, whereas NG314 observed few variations before and relatively large variations after the storm, with a mean of 69 kJ cm^{-2} and standard deviation of 8.6 kJ cm^{-2}, which is mainly explained by the post-storm variations (Fig. 19c). In general, H21H predicted OHC values similar to observations after Laura at NG645 and before Laura at NG314, but large differences with the H21H estimates include $O(21)$ kJ cm^{-2} of overprediction for the pre-storm period at NG645 and 17 kJ cm^{-2} of underprediction for the post-storm period at NG314. The former suggests that H21H lost ~53 kJ cm^{-2} of OHC, which is ~65% more than the observed value (Fig. 19a). Conversely, H3W1 predicted small OHC values at both locations by an average of 26 kJ cm^{-2} (Fig. 19a) and 48 kJ cm^{-2} (Fig. 19c). The storm-induced OHC loss for H3W1 was about 24 kJ cm^{-2}, which is half of the H21H loss and ~75% of the observed magnitude. H3W1 also underpredicted OHC at NG314, with an MD and RMSE of 20 and 9.5 kJ cm^{-2}, respectively. If we consider T100, which is another metric for indicating the available heat in the ocean, proposed by Price (2009), the H3W1 predictions showed relatively good agreement with the observations, with 0.1°C MD and 0.5°C RMSE at NG645 (Fig. 19b), and 0.3° and 0.4°C of MD and RMSE at NG314 (Fig. 19d). However, H21H consistently overestimated T100 at both NG645 and NG314 by an average of 1.3° and 1.0°C, respectively. In summary, H3W1 underestimated z_{26} and OHC. However, H3W1 predicted about the same amount of OHC loss or T100 cooling as the observations. In contrast, H21H overestimated T100, although it had a similar OHC intensity to the observed data. The OHC loss and T100 cooling caused by Laura were predicted well by H3W1 but were overpredicted by H21H.

The H3W1 OHC at the NG645 and NG314 locations was either marginal or smaller than the lower limit (60 kJ cm^{-2}) for the TC support (Mainelli et al. 2008). However, the storm took up as much as 1148.5 W m^{-2} at NG645 for H3W1, but 250 W m^{-2} less than the H21H counterpart (Fig. 19e). This cannot be explained by OHC, because the magnitude is either 60 kJ cm^{-2} or below. Nonetheless, H3W1 still provided 626.6 W m^{-2} heat flux to the storm in spite of only 48 kJ cm^{-2} OHC at the site.

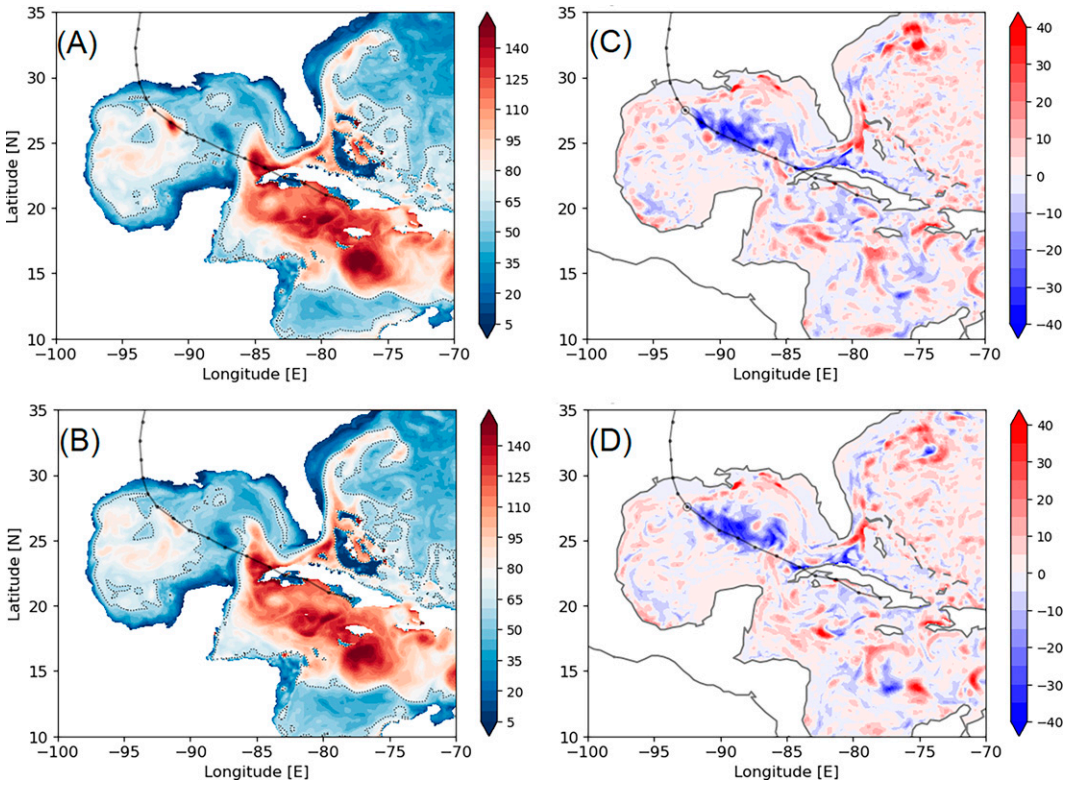

FIG. 18. Initial ocean heat content (OHC; kJ cm^{-2}) for (a) H21H and (b) H3W1, and OHC change at (c),(d) the 60-h lead hour. The dotted black line denotes the predicted track and TC locations at the 6-hourly intervals. The black solid circles in (c) and (d) indicate the 60-h forecast TC location. The dotted contour lines denote 60 kJ cm^{-2}.

e. *Air–sea heat fluxes*

We examined the enthalpy flux and found that the maximum value was located at the radius of maximum wind (Rmax). Figure 20 shows the radial mean flux as a function of the normalized radial distance from a TC center (r/Rmax) for the x axis and forecast lead time from 3 to 78 h before landfall (denoted by a dashed line) for H21A (Fig. 20a), H21H (Fig. 20b), and H3W1 (Fig. 20c). The value is a bin average at every 0.2 r/Rmax. The largest flux was observed at about 51 h for all three runs, but the overall magnitude was the smallest for H3W1, of which the maximum estimate was 1343.2 W m^{-2} and this was 622.3 and 262.2 W m^{-2} lower than the H21A and H21H counterparts, respectively. A similar result was found in terms of the flux variation, showing the magnitude of 81.5 W m^{-2} for H3W1, followed by 104.0 W m^{-2} for H21H, and 136.4 W m^{-2} for H21A.

The time rate of enthalpy flux changes (Figs. 20d–f) suggests two periods of gain. These events appear to share two commonalities of warm SST and slow translation speed, and a difference which is the storm intensity. For the first event, when Laura passes the LC after entering the GOM (18–24 h), the predicted winds (Vmax) are relatively weak, ranging between 55 (H3W1) and 73 kt (H21A), and U_t reaches a local minimum at 12–18 h of 6.0 m s^{-1} (H21A), 7.5 m s^{-1} (H21H), and 6.6 m s^{-1} (H3W1). After the storm reaches a local peak U_t of O(8.5) m s^{-1} over the next 6 h, the storm slows down again. At the time of the second episode (42–54 h), the storm is located over the warm water northwestern GOM, with a Vmax of ≤~85 kt and a U_t of 6.5 m s^{-1}.

In this study, we explicitly focused on employing z_o considering the sea states predicted by WW3, whereas z_t was estimated using Eq. (2) and the z_t–U_{10} fitted curve (appendix B) or the C_k–U_{10} relationship. Because of the weaker U_{10} prediction, the H3W1 heat flux was smaller. In addition, SST cooling induced by the storm was higher due to the enhanced mixing in HYCOM (Fig. 15). The combination of the two processes accounts for the relatively lower heat flux than H21A and H21H.

5. Summary and conclusions

Directional wave coupling and nonlinear interactions in the air–sea interaction zone have been added to the U.S. NCEP's operational HWRF system. In this study, we evaluated the predictability of the full hurricane–ocean–wave coupled system through simulations of Hurricane Laura (2020), by analyzing the performance of each component of the models. For comparison purposes, we included simulations of the atmospheric model (H21A) and the two-way coupled hurricane–ocean system (H21H). The homogeneous validation of all 27 verifiable cases showed performance improvements in track and intensity forecasts of 27% and 17%, respectively, over H21A and of 5% each over H21H. Further analysis suggests

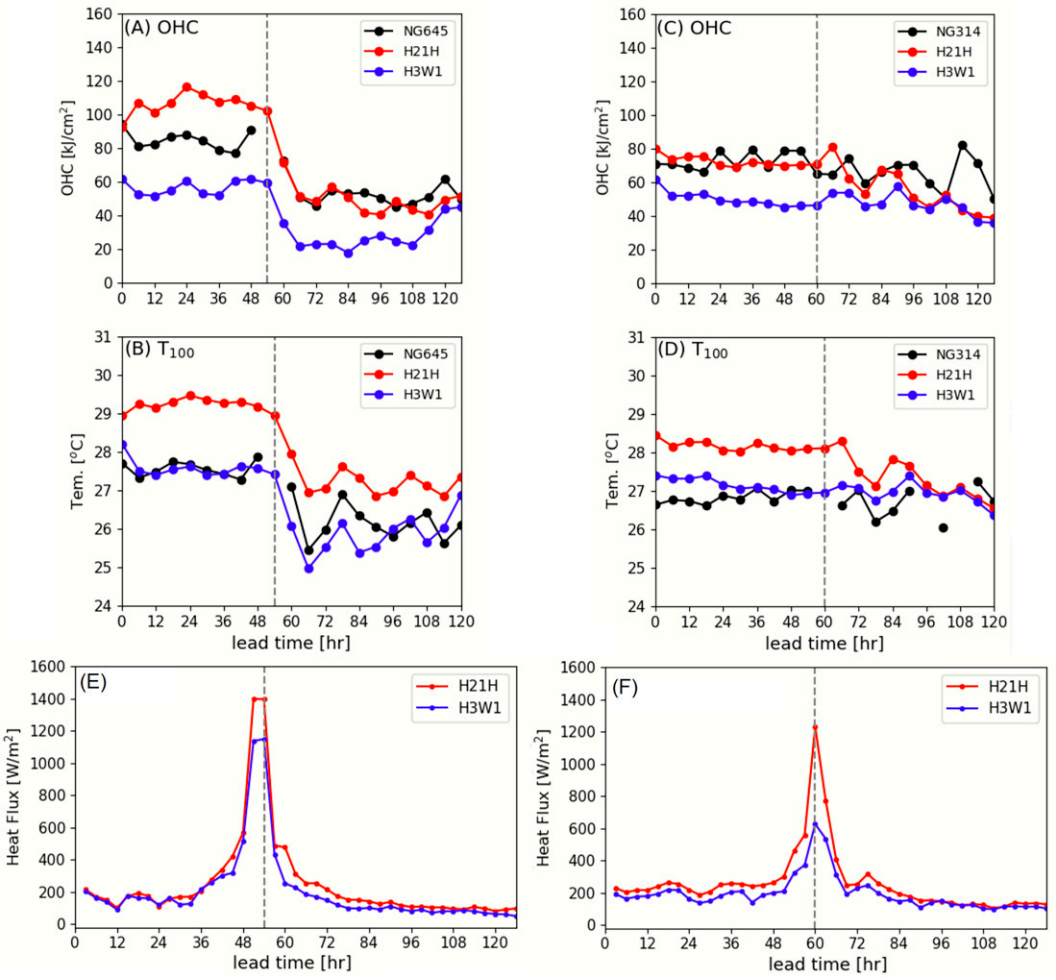

FIG. 19. Comparisons of (a),(c) OHC and (b),(d) T100 between simulations and observations (black dots and line) by NG645 and NG314. Model heat flux estimates at (e) NG645 and (f) NG324. Red and blue dots and lines denote H21H and H3W1, respectively. Vertical dashed lines represent the time when Laura was situated at the closest distance to each site.

that H3W1 shows better predictability of rapid intensification and storm structure.

The storm-induced cooling and SST simulations by dynamic ocean coupling improved the storm intensity, whereas persistent SST employed for the uncoupled atmospheric model resulted in over-intensification. Despite more cooling in the upper ocean, explicit wave coupling further improved the storm intensity, especially delaying premature intensification predicted by the ocean-only coupled and uncoupled system. Because of the underprediction of SST and overprediction of SST cooling, the H4W1 heat flux was 15% and 38% smaller at peak intensity (54 h), for instance, compared to H21H and H21A, respectively. This systematic SST bias, however, little influenced the flux exchanges when the storm passed over the LC, showing the exchanges similar to the estimates with no feedback and twice the magnitude of the two-way coupled estimates.

Simulations of the ocean state showed a reasonable accuracy in representing upper ocean conditions within the model uncertainty of RTOFS (Morris et al. 2016; Ryan et al. 2015). The in-storm glider observations supported the skill improvement in terms of the metrics, except MLD. Because the MLD skill degradation existed for both the H21H and H3W1 simulations (Fig. 13), the Langmuir mixing could be ruled out from the primary controlling parameter, or MLD might be an inapt metric. The T100 evolution in response to the storm agreed with the NDBC buoy observations better than MLD (Fig. 14) and OHC (Fig. 20). Furthermore, the ocean with OHC less than 60 kJ cm^{-2} continued providing the enthalpy flux as much as 1148.5 W m^{-2} (H3W1).

This work demonstrates the numerical advancement of a hurricane forecasting system by including wave coupling and nonlinear interactions between the component models. Unlike recent studies, e.g., Chen et al. (2013) and R14, which have shown quadrant-dependent C_d values, this study shows little variation in space. This was accounted for by employing the scaling of z_o with the sea-state-dependent z_{ow} in the atmospheric surface boundary. The agreement of the model-resolved

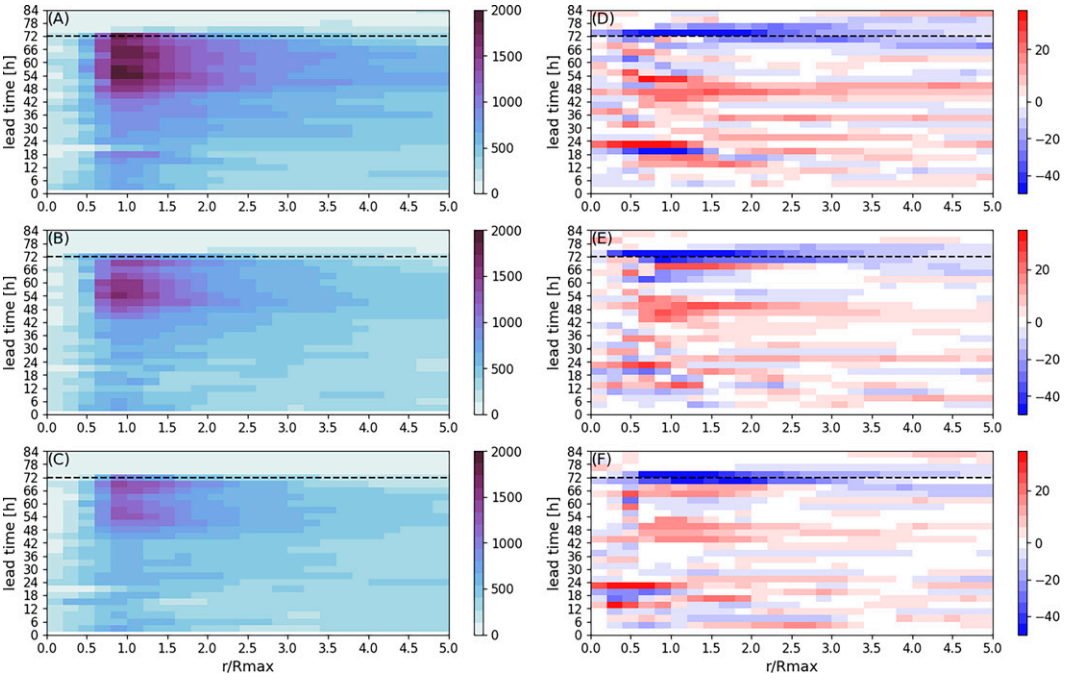

FIG. 20. Enthalpy flux (W m^{-2}) estimated at (a)–(c) the 3-h intervals in a 0.2 binned area and (d)–(f) time rate of the change as a function of the normalized radial distance (r/Rmax) for H21A in (a), H21H in (b), and H3W1 in (c), with lead times (y axis) from 3 to 78 h for the 0600 UTC 24 Aug 2020 cycle. The horizontal dashed line denotes landfall.

wave properties with NDBC buoy observations conversely supports the parameterization of the wave spectral tail in the wave boundary layer. A future effort will be further improvement of air–sea–wave parameterizations, specifically the direct use of z_{ow} and retuning for the full three-way coupling system. Overall, the full atmosphere–ocean–wave coupled forecasts for the case study were encouraging, and the performance evaluated in this study supported the transition to the next-generation operational hurricane prediction system.

Acknowledgments. This work was supported by NOAA's Hurricane Forecast Improvement Project. We thank the NOAA/EMC hurricane model development team and partners from universities and NOAA/AOML for their collective efforts to help to build the forecast system. We especially acknowledge the valuable data support from NOAA National Data Buoy Center and the U.S. IOOS and NOAA National Centers for Environmental Information. The authors express gratitude to reviewers for constructive and helpful suggestions to improve this work.

Data availability statement. The HWRF system code is available at https://svn-dtc-hwrf.cgd.ucar.edu/trunk, and the scientific documentation and user's guide are available at https://dtcenter.org/community-code/hurricane-wrf-hwrf. The model output used in the work is too large to transfer. However, we can make subsets available upon request. To replicate the simulations, we can provide all the information, including configurations and namelist files.

APPENDIX A

Surface Roughness for Momentum Flux (z_o)

This section presents the z_o formula (in m) employed over the sea points in the atmospheric component of the HWRF model, version 2021. A polynomial fitted curve is constructed using different approaches for two major wind ranges. For low to moderate winds, it adopts the C_d and 10-m wind (U_{10} in m s^{-1}) relationship from COARE v3.5 (Edson et al. 2013) and, for high winds, it is fitted to available observational data:

$$z_o = \begin{cases} \exp(p_{10} + p_{11} \times U_{10} + p_{12} \times U_{10}^2 + p_{13} \times U_{10}^3), & \text{for } 0.0 \le U_{10} \le 6.5 \\ \exp(p_{20} + p_{21} \times U_{10} + p_{22} \times U_{10}^2 + p_{23} \times U_{10}^3 + p_{24} \times U_{10}^4 + p_{25} \times U_{10}^5), & \text{for } 6.5 < U_{10} \le 15.7 \\ \exp(p_{30} + p_{31} \times U_{10} + p_{32} \times U_{10}^2 + p_{33} \times U_{10}^3 + p_{34} \times U_{10}^4 + p_{35} \times U_{10}^5), & \text{for } 15.7 < U_{10} \le 53.0 \\ p_{40}, & \text{for } 53.0 < U_{10} \end{cases}$$

where the coefficients are $p_{10} = -8.396\,975\,715\,683\,501 \times 10^{0}$, $p_{11} = -1.597\,898\,515\,251\,717 \times 10^{0}$, $p_{12} = 2.855\,780\,863\,283\,819 \times 10^{-1}$, $p_{13} = -1.296\,521\,881\,682\,694 \times 10^{-2}$, $p_{20} = 2.147\,264\,0203\,694\,13 \times 10^{-5}$, $p_{21} = 1.739\,759\,082\,358\,234 \times 10^{-7}$, $p_{22} = -1.240\,239\,171\,056\,262 \times 10^{-6}$, $p_{23} = 1.962\,282\,433\,562\,894\mathrm{e} \times 10^{-7}$, $p_{24} = 3.281\,964\,357\,650\,687 \times 10^{-9}$, $p_{25} = 3.790\,846\,746\,036\,765 \times 10^{-10}$, $p_{30} = -1.663\,993\,561\,652\,530 \times 10^{1}$, $p_{31} = 1.255\,457\,892\,775\,006 \times 10^{0}$, $p_{32} = -6.139\,315\,534\,216\,305 \times 10^{-2}$, $p_{33} = 1.735\,308\,193\,700\,643 \times 10^{-3}$, $p_{34} = -2.793\,849\,676\,757\,154 \times 10^{-5}$, $p_{35} = 1.840\,430\,200\,185\,075 \times 10^{-7}$, and $p_{40} = 4.579\,369\,142\,033\,410 \times 10^{-4}$.

APPENDIX B

Surface Roughness for Heat Flux (z_t)

This section presents the z_t formula (in m) over the open ocean that was employed in the atmospheric component of the HWRF model, version 2021. A polynomial fitted curve is constructed with different approaches for two major wind ranges. For low to moderate winds, it adopts the C_k value and 10-m wind (U_{10} in m s^{-1}) relationship from COARE v3.5 (Edson et al. 2013) and, for high winds, it retains the C_k and 10-m wind of the 2015 version (Tallapragada et al. 2016):

$$z_t = \begin{cases} p_{00}, & \text{for } 0.0 \le U_{10} \le 5.9 \\ p_{10} + p_{11} \times U_{10} + p_{12} \times U_{10}^2 + p_{13} \times U_{10}^3, & \text{for } 5.9 < U_{10} \le 15.4 \\ p_{20} + p_{21} \times U_{10} + p_{22} \times U_{10}^2 + p_{23} \times U_{10}^3 + p_{24} \times U_{10}^4 + p_{25} \times U_{10}^5, & \text{for } 15.4 < U_{10} \le 21.6 \\ p_{30} + p_{31} \times U_{10} + p_{32} \times U_{10}^2 + p_{33} \times U_{10}^3 + p_{34} \times U_{10}^4 + p_{35} \times U_{10}^5, & \text{for } 21.6 < U_{10} \le 42.6 \\ p_{40} + p_{41} \times U_{10} + p_{42} \times U_{10}^2 + p_{43} \times U_{10}^3 + p_{44} \times U_{10}^4 + p_{45} \times U_{10}^5, & \text{for } 42.6 < U_{10} \le 51.5 \\ p_{50} + p_{51} \times U_{10} + p_{52} \times U_{10}^2 + p_{53} \times U_{10}^3 + p_{54} \times U_{10}^4 + p_{55} \times U_{10}^5, & \text{for } 51.5 < U_{10} \le 80.0 \\ p_{60}, & \text{for } 80.0 < U_{10}, \end{cases}$$

where the coefficients are $p_{00} = 1.100\,000\,000\,000\,000 \times 10^{-4}$, $p_{10} = 8.644\,979\,973\,037\,803 \times 10^{-4}$, $p_{11} = -2.633\,566\,691\,328\,004 \times 10^{-4}$, $p_{12} = 3.342\,963\,077\,911\,962 \times 10^{-5}$, $p_{13} = -2.163\,419\,217\,747\,114 \times 10^{-6}$, $p_{14} = 7.052\,217\,518\,653\,943 \times 10^{-8}$, $p_{15} = -9.193\,764\,479\,895\,316 \times 10^{-10}$, $p_{20} = 1.484\,341\,646\,128\,200 \times 10^{-4}$, $p_{21} = -2.680\,293\,455\,916\,390 \times 10^{-5}$, $p_{22} = 1.982\,901\,461\,144\,764 \times 10^{-6}$, $p_{23} = -7.299\,148\,051\,141\,852 \times 10^{-8}$, $p_{24} = 1.325\,396\,583\,616\,614 \times 10^{-9}$, $p_{25} = -9.40\,272\,245\,0219\,142 \times 10^{-12}$, $p_{30} = -7.558\,911\,792\,344\,770 \times 10^{-5}$, $p_{31} = 1.659\,454\,106\,237\,737 \times 10^{-5}$, $p_{32} = -1.337\,841\,892\,062\,716 \times 10^{-6}$, $p_{33} = 5.251\,986\,927\,351\,103 \times 10^{-8}$, $p_{34} = -1.019\,028\,029\,546\,602 \times 10^{-9}$, $p_{35} = 7.921\,446\,674\,311\,864 \times 10^{-12}$, $p_{40} = 3.951\,492\,707\,214\,883 \times 10^{-2}$, $p_{41} = -4.617\,267\,288\,861\,201 \times 10^{-3}$, $p_{42} = 2.156\,326\,523\,752\,734 \times 10^{-4}$, $p_{43} = -5.027\,577\,045\,502\,003 \times 10^{-6}$, $p_{44} = 5.845\,859\,022\,891\,930 \times 10^{-8}$, $p_{45} = -2.706\,461\,188\,613\,193 \times 10^{-10}$, $p_{50} = -9.027\,924\,333\,673\,693 \times 10^{-3}$, $p_{51} = 8.407\,596\,231\,678\,149 \times 10^{-4}$, $p_{52} = -3.206\,421\,106\,713\,471 \times 10^{-5}$, $p_{53} = 6.493\,685\,149\,526\,543 \times 10^{-7}$, $p_{54} = -7.375\,373\,918\,500\,171 \times 10^{-9}$, $p_{55} = 4.450\,334\,755\,105\,140 \times 10^{-11}$, $p_{56} = -1.112\,896\,580\,069\,263 \times 10^{-13}$, and $p_{60} = 5.791\,179\,079\,892\,191 \times 10^{-5}$.

REFERENCES

Ali, A., K. H. Christensen, Ø. Breivik, M. Malila, R. P. Raj, L. Bertino, E. P. Chassignet, and M. Bakhoday-Paskyabi, 2019: A comparison of Langmuir turbulence parameterizations and key wave effects in a numerical model of the North Atlantic and Arctic Oceans. *Ocean Modell.*, **137**, 76–97, https://doi.org/10.1016/j.ocemod.2019.02.005.

Ardhuin, F., and Coauthors, 2010: Semiempirical dissipation source functions for ocean waves. Part I: Definition, calibration, and validation. *J. Phys. Oceanogr.*, **40**, 1917–1941, https://doi.org/10.1175/2010JPO4324.1.

Banzon, V., T. M. Smith, T. M. Chin, C. Liu, and W. Hankins, 2016: A long-term record of blended satellite and in situ sea-surface temperature for climate monitoring, modeling and environmental studies. *Earth Syst. Sci. Data*, **8**, 165–176, https://doi.org/10.5194/essd-8-165-2016.

Bender, M. A., I. Ginis, R. Tuleya, B. Thomas, and T. Marchok, 2007: The operational GFDL coupled hurricane–ocean prediction system and a summary of its performance. *Mon. Wea. Rev.*, **135**, 3965–3989, https://doi.org/10.1175/2007MWR2032.1.

Benetazzo, A., S. Carniel, M. Sclavo, and A. Bergamasco, 2013: Wave–current interaction: Effect on the wave field in a semi-enclosed basin. *Ocean Modell.*, **70**, 152–165, https://doi.org/10.1016/j.ocemod.2012.12.009.

Biswas, M. K., and Coauthors, 2018: Hurricane Weather Research and Forecasting (HWRF) Model: 2018 Scientific Documentation. Developmental Testbed Center, 112 pp., https://dtcenter.org/sites/default/files/community-code/hwrf/docs/scientific_documents/HWRFv4.0a_ScientificDoc.pdf.

Black, P. G., and Coauthors, 2007: Air–sea exchange in hurricanes: Synthesis of observations from the Coupled Boundary Layer Air–Sea Transfer Experiment. *Bull. Amer. Meteor. Soc.*, **88**, 357–374, https://doi.org/10.1175/BAMS-88-3-357.

Bleck, R., 2002: An oceanic general circulation model framed in hybrid isopycnic-Cartesian coordinates. *Ocean Modell.*, **4**, 55–88, https://doi.org/10.1016/S1463-5003(01)00012-9.

——, and D. B. Boudra, 1981: Initial testing of a numerical ocean circulation model using a hybrid (quasi-isopycnic) vertical coordinate. *J. Phys. Oceanogr.*, **11**, 755–770, https://doi.org/10.1175/1520-0485(1981)011<0755:ITOANO>2.0.CO;2.

Brand, S., 1971: The effects on a tropical cyclone of cooler surface waters due to upwelling and mixing produced by a prior tropical cyclone. *J. Appl. Meteor.*, **10**, 865–874, https://doi.org/10.1175/1520-0450(1971)010<0865:TEOATC>2.0.CO;2.

Bye, J. A. T., and J.-O. Wolff, 2008: Charnock dynamics: A model for the velocity structure in the wave boundary layer of the air–sea interface. *Ocean Dyn.*, **58**, 31–42, https://doi.org/10.1007/s10236-007-0130-5.

Chao, Y. Y., J. H. G. Alves, and H. L. Tolman, 2005: An operational system for predicting hurricane-generated wind waves

in the North Atlantic Ocean. *Wea. Forecasting*, **20**, 652–671, https://doi.org/10.1175/WAF851.1.

Charnock, H., 1955: Wind stress on a water surface. *Quart. J. Roy. Meteor. Soc.*, **81**, 639–640, https://doi.org/10.1002/qj.49708135027.

Chassignet, E. P., L. T. Smith, G. R. Halliwell, and R. Bleck, 2003: North Atlantic simulations with the Hybrid Coordinate Ocean Model (HYCOM): Impact of the vertical coordinate choice, reference pressure, and thermobaricity. *J. Phys. Oceanogr.*, **33**, 2504–2526, https://doi.org/10.1175/1520-0485(2003)033<2504:NASWTH>2.0.CO;2.

Chen, S. S., J. F. Price, W. Zhao, M. A. Donelan, and E. J. Walsh, 2007: The CBLAST-Hurricane program and the next-generation fully coupled atmosphere–wave–ocean models for hurricane research and prediction. *Bull. Amer. Meteor. Soc.*, **88**, 311–318, https://doi.org/10.1175/BAMS-88-3-311.

——, W. Zhao, M. A. Donelan, and H. L. Tolman, 2013: Directional wind–wave coupling in fully coupled atmosphere–wave–ocean models: Results from CBLAST-Hurricane. *J. Atmos. Sci.*, **70**, 3198–3215, https://doi.org/10.1175/JAS-D-12-0157.1.

Donelan, M. A., B. K. Haus, N. Reul, W. J. Plant, M. Stiassnie, H. C. Graber, O. B. Brown, and E. S. Saltzman, 2004: On the limiting aerodynamic roughness of the ocean in very strong winds. *Geophys. Res. Lett.*, **31**, L18306, https://doi.org/10.1029/2004GL019460.

Doyle, J. D., 2002: Coupled atmosphere–ocean wave simulations under high wind conditions. *Mon. Wea. Rev.*, **130**, 3087–3099, https://doi.org/10.1175/1520-0493(2002)130<3087:CAOWSU>2.0.CO;2.

——, and Coauthors, 2012: Real-time tropical cyclone prediction using COAMPS-TC. *Advances in Geosciences: Volume 28: Atmospheric Science (AS) and Ocean Science (OS)*, K. Satake, C.-C. Wu, J. Gan, Eds., World Scientific, 15–28.

——, and Coauthors, 2014: Tropical cyclone prediction using COAMPS-TC. *Oceanography*, **27**, 104–115, https://doi.org/10.5670/oceanog.2014.72.

Edson, J. B., and Coauthors, 2007: The Coupled Boundary Layers and Air-Sea Transfer Experiment in low winds. *Bull. Amer. Meteor. Soc.*, **88**, 341–356, https://doi.org/10.1175/BAMS-88-3-341.

——, and Coauthors, 2013: On the exchange of momentum over the open ocean. *J. Phys. Oceanogr.*, **43**, 1589–1610, https://doi.org/10.1175/JPO-D-12-0173.1.

Fairall, C. W., E. F. Bradley, J. E. Hare, A. A. Grachev, and J. B. Edson, 2003: Bulk parameterization of air–sea fluxes: Updates and verification for the COARE algorithm. *J. Climate*, **16**, 571–591, https://doi.org/10.1175/1520-0442(2003)016<0571:BPOASF>2.0.CO;2.

Ferrier, B. S., Y. Jin, Y. Lin, T. Black, E. Rogers, and G. DiMego, 2002: Implementation of a new grid-scale cloud and precipitation scheme in the NCEP Eta model. *19th Conf. on Weather Analysis and Forecasting/15th Conf. on Numerical Weather Prediction*, San Antonio, TX, Amer. Meteor. Soc., 10.1, https://ams.confex.com/ams/SLS_WAF_NWP/techprogram/paper_47241.htm.

Gopalakrishnan S. G., Q. Liu, T. Marchok, D. Sheinin, N. Surgi, R. Tuleya, R. Yablonsky, and X. Zhang, 2011: Hurricane Weather Research and Forecasting (HWRF) Model: 2011 scientific documentation. NOAA/NCAR/Development Testbed Center, 81 pp.

Hagos, S., and Coauthors, 2020: Atmospheric convection and air–sea interactions over the tropical oceans: Scientific progress, challenges, and opportunities. *Bull. Amer. Meteor. Soc.*, **101**, E253–E258, https://doi.org/10.1175/BAMS-D-19-0261.1.

Halliwell, G. R., 2004: Evaluation of vertical coordinate and vertical mixing algorithms in the HYbrid-Coordinate Ocean Model (HYCOM). *Ocean Modell.*, **7**, 285–322, https://doi.org/10.1016/j.ocemod.2003.10.002.

Han, J., and H.-L. Pan, 2011: Revision of convection and vertical diffusion schemes in the NCEP Global Forecast System. *Wea. Forecasting*, **26**, 520–533, https://doi.org/10.1175/WAF-D-10-05038.1.

Hara, T., and S. E. Belcher, 2002: Wind forcing in the equilibrium range of wind-wave spectra. *J. Fluid Mech.*, **470**, 223–245, https://doi.org/10.1017/S0022112002001945.

Harcourt, R. R., and E. A. D'Asaro, 2008: Large-eddy simulation of Langmuir turbulence in pure wind seas. *J. Phys. Oceanogr.*, **38**, 1542–1562, https://doi.org/10.1175/2007JPO3842.1.

Hegermiller, C. A., J. C. Warner, M. Olabarrieta, and C. R. Sherwood, 2019: Wave–current interaction between Hurricane Matthew wave fields and the Gulf Stream. *J. Phys. Oceanogr.*, **49**, 2883–2900, https://doi.org/10.1175/JPO-D-19-0124.1.

Holthuijsen, L. H., M. D. Powell, and J. D. Pietrzak, 2012: Wind and waves in extreme hurricanes. *J. Geophys. Res.*, **117**, C09003, https://doi.org/10.1029/2012JC007983.

Hsu, J. Y., R. C. Lien, E. A. D'Asaro, and T. B. Sanford, 2017: Estimates of surface wind stress and drag coefficients in Typhoon Megi. *J. Phys. Oceanogr.*, **47**, 545–565, https://doi.org/10.1175/JPO-D-16-0069.1.

Iacono, M. J., J. S. Delamere, E. J. Mlawer, M. W. Shephard, S. A. Clough, and W. D. Collins, 2008: Radiative forcing by long-lived greenhouse gases: Calculations with the AER radiative transfer models. *J. Geophys. Res.*, **113**, D13103, https://doi.org/10.1029/2008JD009944.

Janjić, Z. I., R. Gall, and M. E. Pyle, 2010: Scientific documentation for the NMM solver. NCAR Tech. Note NCAR/TN-477+STR, 54 pp, https://doi.org/10.5065/D6MW2F3Z.

Kim, H.-S., C. Lozano, V. Tallapragada, D. Iredell, D. Sheinin, H. L. Tolman, V. M. Gerald, and J. Sims, 2014: Performance of ocean simulations in the coupled HWRF–HYCOM model. *J. Atmos. Oceanic Technol.*, **31**, 545–559, https://doi.org/10.1175/JTECH-D-13-00013.1.

Kudryavtsev, V. N., and V. K. Makin, 2001: The impact of airflow separation on the drag of the sea surface. *Bound.-Layer Meteor.*, **98**, 155–171, https://doi.org/10.1023/A:1018719917275.

Kurihara, Y., R. E. Tuleya, and M. A. Bender, 1998: The GFDL hurricane prediction system and its performance in the 1995 hurricane season. *Mon. Wea. Rev.*, **126**, 1306–1322, https://doi.org/10.1175/1520-0493(1998)126<1306:TGHPSA>2.0.CO;2.

Large, W. G., J. C. McWilliams, and S. C. Doney, 1994: Oceanic vertical mixing: A review and a model with a nonlocal boundary layer parameterization. *Rev. Geophys.*, **32**, 363–403, https://doi.org/10.1029/94RG01872.

Leipper, D. F., and D. Volgenau, 1972: Hurricane heat potential of the Gulf of Mexico. *J. Phys. Oceanogr.*, **2**, 218–224, https://doi.org/10.1175/1520-0485(1972)002<0218:HHPOTG>2.0.CO;2.

Liu, B., H. Liu, L. Xie, C. Guan, and D. Zhao, 2011: A coupled atmosphere–wave–ocean modeling system: Simulation of the intensity of an idealized tropical cyclone. *Mon. Wea. Rev.*, **139**, 132–152, https://doi.org/10.1175/2010MWR3396.1.

Mainelli, M., M. DeMaria, L. K. Shay, and G. Goni, 2008: Application of oceanic heat content estimation to operational forecasting of recent Atlantic category-5 hurricanes. *Wea. Forecasting*, **23**, 3–16, https://doi.org/10.1175/2007WAF2006111.1.

Makin, V. K., and V. N. Kudryavtsev, 2002: Impact of dominant waves on sea drag. *Bound.-Layer Meteor.*, **103**, 83–99, https://doi.org/10.1023/A:1014591222717.

McWilliams, J. C., and P. P. Sullivan, 2000: Vertical mixing by Langmuir circulations. *Spill Sci. Technol. Bull.*, **6**, 225–237, https://doi.org/10.1016/S1353-2561(01)00041-X.

Mehra, A., V. Tallapragada, Z. Zhang, B. Liu, L. Zhu, W. Wang, and H.-S. Kim, 2018: Advancing the state of the art in operational tropical cyclone forecasting at NCEP. *Trop. Cyclone Res. Rev.*, **7**, 51–56, https://doi.org/10.6057/2018TCRR01.06.

Moon, I.-J., T. Hara, I. Ginis, S. E. Belcher, and H. Tolman, 2004a: Effect of surface waves on air–sea momentum exchange. Part I: Effect of mature and growing seas. *J. Atmos. Sci.*, **61**, 2321–2333, https://doi.org/10.1175/1520-0469(2004)061<2321:EOSWOA>2.0.CO;2.

——, I. Ginis, and T. Hara, 2004b: Effect of surface waves on air–sea momentum exchange. Part II: Behavior of the drag coefficient under tropical cyclones. *J. Atmos. Sci.*, **61**, 2334–2348, https://doi.org/10.1175/1520-0469(2004)061<2334:EOSWOA>2.0.CO;2.

Morrison, A., and Coauthors, 2016: Model comparison for transatlantic ocean glider flight: Student analysis of modern circumnavigation. *OCEANS 2015—MTS/IEEE Washington*, Washington, DC, Institute of Electrical and Electronics Engineers, 1–7, https://doi.org/10.23919/OCEANS.2015.7404505.

Porchetta, S., O. Temel, J. C. Warner, D. Muñoz-Esparza, J. Monbaliu, J. van Beeck, and N. van Lipzig, 2020: Evaluation of a roughness length parametrization accounting for wind-wave alignment in a coupled atmosphere-wave model. *Quart. J. Roy. Meteor. Soc.*, **147**, 825–846, https://doi.org/10.1002/qj.3948.

Price, J. F., 2009: Metrics of hurricane-ocean interaction: Vertically-integrated or vertically-averaged ocean temperature? *Ocean Sci.*, **5**, 351–368, https://doi.org/10.5194/os-5-351-2009.

Reichl, B., T. Hara, and I. Ginis, 2014: Sea state dependence of the wind stress over the ocean under hurricane winds. *J. Geophys. Res. Oceans*, **119**, 30–51, https://doi.org/10.1002/2013JC009289.

——, D. Wang, T. Hara, I. Ginis, and T. Kukulka, 2016: Langmuir turbulence parameterization in tropical cyclone conditions. *J. Phys. Oceanogr.*, **46**, 863–886, https://doi.org/10.1175/JPO-D-15-0106.1.

Renault, L., M. J. Molemaker, J. C. McWilliams, A. F. Shchepetkin, F. Lemarié, D. Chelton, S. Illig, and A. Hall, 2016: Modulation of wind work by oceanic current interaction with the atmosphere. *J. Phys. Oceanogr.*, **46**, 1685–1704, https://doi.org/10.1175/JPO-D-15-0232.1.

Reynolds, R. W., T. M. Smith, C. Y. Liu, D. B. Chelton, K. S. Casey, and M. G. Schlax, 2007: Daily high-resolution-blended analyses for sea surface temperature. *J. Climate*, **20**, 5473–5496, https://doi.org/10.1175/2007JCLI1824.1.

Rogers, W. E., and A. J. Wallcraft, 2013: Develop and test coupled physical parameterizations and tripolar wave model grid: NAVGEM/WaveWatch III/HYCOM. NRL Rep. 2013-09-30, 9 pp., https://apps.dtic.mil/sti/citations/ADA601275.

Ryan, A. G., and Coauthors, 2015: GODAE OceanView Class 4 forecast verification framework: Global ocean inter-comparison. *J. Oper. Oceanogr.*, **8**, s98–s111, https://doi.org/10.1080/1755876X.2015.1022330.

Sandery, P. A., G. B. Brassington, A. Craig, and T. Pugh, 2010: Impacts of ocean–atmosphere coupling on tropical cyclone intensity change and ocean prediction in the Australian region. *Mon. Wea. Rev.*, **138**, 2074–2091, https://doi.org/10.1175/2010MWR3101.1.

Shay, L. K., and E. W. Uhlhorn, 2008: Loop current response to Hurricanes Isidore and Lili. *Mon. Wea. Rev.*, **136**, 3248–3274, https://doi.org/10.1175/2007MWR2169.1.

——, P. G. Black, A. J. Mariano, J. D. Hawkins, and R. L. Elsberry, 1992: Upper ocean response to Hurricane Gilbert. *J. Geophys. Res.*, **97**, 20 227–20 248, https://doi.org/10.1029/92JC01586.

——, G. J. Goni, and P. G. Black, 2000: Effects of a warm oceanic feature on Hurricane Opal. *Mon. Wea. Rev.*, **128**, 1366–1383, https://doi.org/10.1175/1520-0493(2000)128<1366:EOAWOF>2.0.CO;2.

Small, R. D., and Coauthors, 2008: Air–sea interaction over ocean fronts and eddies. *Dyn. Atmos. Oceans*, **45**, 274–319, https://doi.org/10.1016/j.dynatmoce.2008.01.001.

Smyth, W. D., E. D. Skyllingstad, G. B. Crawford, and H. Wijesekera, 2002: Nonlocal fluxes and Stokes drift effects in the K-profile parameterization. *Ocean Dyn.*, **52**, 104–115, https://doi.org/10.1007/s10236-002-0012-9.

Song, X., 2021: The importance of including sea surface current when estimating air–sea turbulent heat fluxes and wind stress in the Gulf Stream region. *J. Atmos. Oceanic Technol.*, **38**, 119–138, https://doi.org/10.1175/JTECH-D-20-0094.1.

Sweet, W., R. Fett, J. Kerling, and P. La Violette, 1981: Air–sea interaction effects in the lower troposphere across the north wall of the Gulf Stream. *Mon. Wea. Rev.*, **109**, 1042–1052, https://doi.org/10.1175/1520-0493(1981)109<1042:ASIEIT>2.0.CO;2.

Takaya, Y., J.-R. Bidlot, A. C. M. Beljaars, and P. A. E. M. Janssen, 2010: Refinements to a prognostic scheme of skin sea surface temperature. *J. Geophys. Res.*, **115**, C06009, https://doi:10.1029/2009JC005985.

Tallapragada, V., 2016: Overview of the NOAA/NCEP Operational Hurricane Weather Research and Forecast (HWRF) modelling system. *Advanced Numerical Modeling and Data Assimilation Techniques for Tropical Cyclone Prediction*, U. Mohanty and S. G. Gopalakrishnan, Eds., Springer, 51–106.

——, and Coauthors, 2016: Hurricane Weather Research and Forecasting (HWRF) Model: 2015 scientific documentation. NCAR Tech. Note NCAR/TN-522+STR, 119 pp, https://doi.org/10.5065/D6ZP44B5.

Tolman, H. L., 2014: User manual and system documentation of WAVEWATCH III version 4.18. NOAA/NWS/NCEP/MMAB Tech. Note 316, NOAA, 194 pp.

Wallcraft, A. J., E. J. Metzger, and S. N. Carroll, 2009: Software design description for the hybrid coordinate ocean model (HYCOM), version 2.2. NRL/MR/7320-09-9166, NRL, 149 pp.

Wang, W., B. Liu, L. Zhu, Z. Zhang, A. Mehra, and V. Tallapragada, 2021: A new horizontal mixing-length formulation for numerical simulations of tropical cyclones. *Wea. Forecasting*, **36**, 679–695, https://doi.org/10.1175/WAF-D-20-0134.1.

Xu, X., J. J. Voermans, Q. Liu, I. J. Moon, C. Guan, and A. V. Babanin, 2021: Impacts of the wave-dependent sea spray parameterizations on air–sea–wave coupled modeling under an idealized tropical cyclone. *J. Mar. Sci. Eng.*, **9**, 1390, https://doi.org/10.3390/jmse9121390.

Zambon, J. B., R. He, and J. C. Warner, 2014: Investigation of Hurricane Ivan using the Coupled Ocean–Atmosphere–Wave–Sediment Transport (COAWST) Model. *Ocean Dyn.*, **64**, 1535–1554, https://doi.org/10.1007/s10236-014-0777-7.

——, ——, ——, and C. A. Hegermiller, 2021: Impact of SST and surface waves on Hurricane Florence (2018): A coupled

modeling investigation. *Wea. Forecasting*, **36**, 1713–1734, https://doi.org/10.1175/WAF-D-20-0171.1.

Zhang, J. A., and F. D. Marks, 2015: Effects of horizontal diffusion on tropical cyclone intensity change and structure in idealized three-dimensional numerical simulations. *Mon. Wea. Rev.*, **143**, 3981–3995, https://doi.org/10.1175/MWR-D-14-00341.1.

——, R. F. Rogers, D. S. Nolan, and F. D. Marks, 2011: On the characteristic height scales of the hurricane boundary layer. *Mon. Wea. Rev.*, **139**, 2523–2535, https://doi.org/10.1175/MWR-D-10-05017.1.

——, D. S. Nolan, R. F. Rogers, and V. Tallapragada, 2015: Evaluating the impact of improvements in the boundary layer parameterization on hurricane intensity and structure forecasts in HWRF. *Mon. Wea. Rev.*, **143**, 3136–3155, https://doi.org/10.1175/MWR-D-14-00339.1.

——, F. D. Marks, J. A. Sippel, R. F. Rogers, X. Zhang, S. G. Gopalakrishnan, Z. Zhang, and V. Tallapragada, 2018: Evaluating the impact of improvement in the horizontal diffusion parameterization on hurricane prediction in the operational Hurricane Weather Research and Forecast (HWRF) Model. *Wea. Forecasting*, **33**, 317–329, https://doi.org/10.1175/WAF-D-17-0097.1.